ABSTRACT

SYNOPTIC VARIABILITY OF A CIR-DRIVEN OPEN-CLOSED BOUNDARY DURING SOLAR MINIMUM

by
Kevin Urban

The year 2008 marked a historically quiet period of solar activity during the declining phase of solar cycle 23. Such quiet time has permitted researchers to clearly distinguish the spectral signature of a corotating interaction region's (CIR) impact on the open-closed boundary (OCB) of the magnetosphere in the southern hemisphere's auroral zone. By using the PENGUIn AGOs network of ground-based magnetometers on the Antarctic continent, the synoptic behavior of the OCB during a CIR-driven magnetic storm has been studied. Observations were compared with results provided by the BATSRUS space weather model. It is shown that such synoptic magnetometer data sets of the OCB during these storms allows for a careful test of current space weather models.

SYNOPTIC VARIABILITY OF A CIR-DRIVEN OPEN-CLOSED BOUNDARY DURING SOLAR MINIMUM

by
Kevin Urban

A Thesis
Submitted to the Faculty of
New Jersey Institute of Technology
in Partial Fulfillment of the Requirements for the Degree of
Master of Science in Applied Physics

Department of Physics

August 2010

APPROVAL PAGE

SYNOPTIC VARIABILITY OF A CIR-DRIVEN OPEN-CLOSED BOUNDARY DURING SOLAR MINIMUM

Kevin Urban

Andrew Gerrard, Thesis Advisor — Date
Associate Professor, Department of Physics, NJIT

Dr. Louis J. Lanzerotti, Committee Member — Date
Distinguished Research Professor, Department of Physics, NJIT

Dr. Dale E. Gary, Committee Member — Date
Distinguished Professor, Department of Physics, NJIT

BIOGRAPHICAL SKETCH

Author: Kevin Urban

Degree: Master of Science

Date: August 2010

Undergraduate and Graduate Education:

- Master of Science in Applied Physics,
  New Jersey Institute of Technology, Newark, NJ, 2010

- Bachelor of Science in Applied Physics,
  New Jersey Institute of Technology, Newark, NJ, 2010

Major: Applied Physics

Presentations and Publications:

Urban, K. and A. J. Gerrard, Space Weather Research at the UACNJ Field Site: How UACNJ Helps NJIT and Antarctic Research, United Astronomy Clubs of New Jersey, July 19, 2008.

To Mrs. Kaicher, my high school public speaking teacher, who was able to see past all my teen angst and delinquency, who told me I'd go far when everyone else was saying otherwise. To Mr. Beaver, my high school algebra teacher, for all those Snickers™ bars I won solving supposedly hard math problems—a year later, in the midst of turmoil and confusion, this memory became my impetus and vision of my place in the world. To Dr. Gradone, my music theory teacher at the County College of Morris, who spelled 'fish' G-H-O-T-I-O and who made sure we all appreciated how bizarre and amazing it is that we have running water in our homes. To Dr. Dale Gary, without whom I would have not had the incredible opportunity to intern at NASA as an undergraduate. To Dr. Denis Blackmore, who has been an extraordinary mentor, comrade, and inspiration throughout my education. To Dr. Andrew Gerrard, who has supported and guided me over these past few years, and who has pushed me to understand the technical difficulties of scientific investigation head on. I cannot thank Dr. Gerrard enough for encouraging me to stick around for graduate school; it was the challenge of the graduate level physics courses, with the quick, tantalizing glimpses of mathematical landscapes previously foreign to me, that opened up my eyes to my most central passion: mathematics, not merely as a means, but as an end in and of itself.

Most importantly, to my parents who have made this possible for me; I can't thank them enough for not forcing me to go to college. To my girlfriend, Jackie, who has put up with me throughout my graduate studies—even though she periodically felt I loved math and physics more than her. To my twin brother, John, with whom I most often discuss philosophical and scientific matters, and from who I stole DNA to use as my own—it's been working out pretty well for me, thank you.

ACKNOWLEDGMENT

I would like to acknowledge the following, for whom much of the success of this project is owed: Dr. Andrew Gerrard, my thesis advisor, who has guided me skillfully in my research; Dr. Louis J. Lanzerotti, committee member, whose research has made my own possible, and who helped at a critical moment in my writing; Dr. Bob Melville, field engineer for PENGUIn AGOs, who is responsible for making sure our instruments in Antarctica function properly year after year; Dr. Dale Gary, committee member, for his time and effort on behalf of this thesis; Gil Jeffer, the United Astronomy Clubs of New Jersey (UACNJ), and Jenny Jump State forest, for their participation in our research efforts; Aaron Ridley, of the University of Michigan, for his time, patience, and modeling efforts on our behalf; my lab mates, Mandeep Singh, Dhvanit Mehta, John King, Zhaozhao Li, Salman Naqvi, and Anthony Teti; and Christine Oertel and everyone else at the Center for Solar-Terrestrial Research.

TABLE OF CONTENTS

TABLE OF CONTENTS
(Continued)

LIST OF TABLES

LIST OF FIGURES

LIST OF FIGURES
(Continued)

LIST OF FIGURES
(Continued)

LIST OF FIGURES
(Continued)

Figure **Page**

CHAPTER 1

INTRODUCTION

1.1 Space Weather

High above the Earth's lower and middle atmosphere there exists a spread of dynamical conditions characterizing what has become known as space weather. In the manner that "weather" entails the myriad conditions and dynamically changing environment of the troposphere, the phrase "space weather" refers to the conditions and on-going transformations of the near-space environment—often referred to as geospace—which includes such realms as the ionosphere, magnetosphere, and plasmasphere. Beyond the terrestrial similarities, "space weather" also refers to the present conditions at the surface of the sun and to a continuous solar output of charged particles, supersonically in transit, known as the solar wind.

Roughly speaking, space weather as a science is the study of plasmas in various environments, under a diverse host of conditions. The solar wind, coronal mass ejections (CMEs), solar flares, corotating interaction regions (CIRs), the matter of the ionosphere and magnetosphere—these are all plasmas. By better understanding these plasmas and their interactions, scientists are better able to forecast tomorrow's space weather. This is becoming ever more important as society continually grows dependent on satellite-based communications and the global positioning system (GPS), an infrastructure susceptible to the ample assault of radiation and highly variable electromagnetic fields inherent in the dynamical content of the solar wind. Space weather will continue to grow in importance as the emerging enterprise of space tourism and progressive human-based space missions become more prevalent, as forecasts will be able to serve as warnings of incoming solar

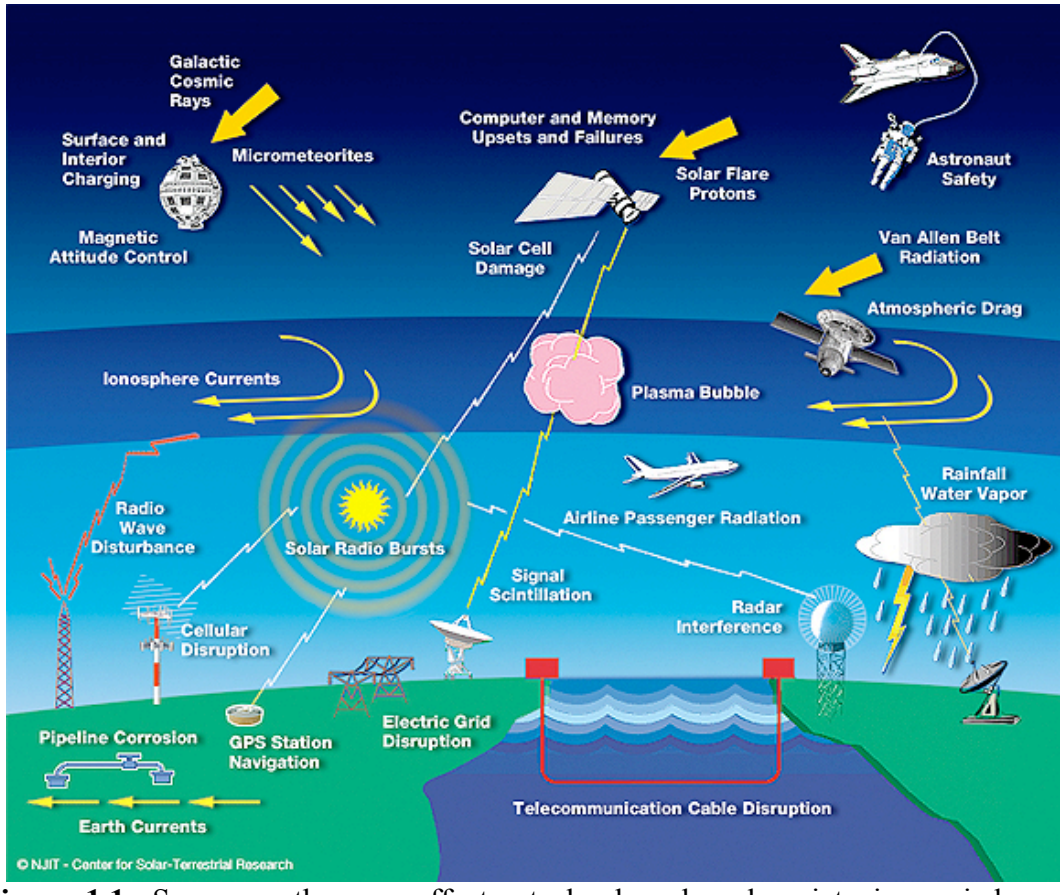

Figure 1.1 Space weather can affect a technology-based society in myriad ways, which include disruptions of telecommunications, satellite damage, and astronaut safety.

(Image Credit: Louis Lanzerotti, John Oertel.)

events, such as coronal mass ejections, which contain deadly doses of radiation.

The prevailing element of all space weather is the solar wind. Originating in the solar corona, it is a radial outward super-Alfenic flow of plasma consisting mostly of protons, electrons, and helium nuclei.

While now known to be an absolutely fundamental connection between the Sun and Earth, the solar wind was far from an obvious one.

One of the first realizations of this connection was in 1859 when Richard Carrington, while studying sunspots, abruptly noticed a bright blemish develop within one of his specimens—about a day later, a large geomagnetic storm was recorded. Could it be that the storm was owed to this odd phenomenon Carrington witnessed? Many of Carrington's colleagues considered this connection highly unlikely, yet enough curiosity was piqued that over time, through observation and theoretical development, a handful of scientists established that a sun-earth connection, other than the sun's provision of optical light, was a physically tenable notion and ultimately that it did indeed exist.

One such scientist, Kristian Birkeland, in the early 1900's dared to conjecture that the Earth isn't merely bombarded by periodic bursts from the sun (as Carrington had suggested), but is likely to be continuously showered by an incessant liberation of charged particles. He showed, using a clever experiment in which he aimed an electron beam at a magnetized ball representing Earth (an object known as a "terrella"), that the aurora of Earth's polar regions is plausibly created by a continuous stream of charged particles.

By the 1950's, it had been reasoned that the solar corona must be on the order of a million degrees (three orders of magnitude greater than the temperature of the layer

below it, known as the photosphere). Sydney Chapman, a British mathematician, computed the properties of a gas at such a temperature and showed that the solar corona must expand further than even Earth's orbit. During the same time period, it was also proposed that the reason comet tails strictly face away from the Sun is due to an unrelenting solar discharge of particles. Eugene Parker, an American solar physicist, argued that the two concepts described one physical entity—something he called the "solar wind."

The solar wind is typically categorized into two major types: fast and slow. The slow wind is typically on the order of 400 km/s (~ one million miles per hour), while the fast wind is approximately double that speed. This is definitely an oversimplification, especially during times surrounding solar maximum when a highly variable slow wind becomes dominant. However, during solar minimum—the focus of this thesis—the categorization is crude but appropriate, the distinction being quite clear.

One might presuppose that a slower wind is associated with a calmer Sun—it does not seem unreasonable that a slow wind would prevail when not "enhanced" by some kind of explosive disturbance. But this is incorrect. The fast wind most typically characterizes the "ground state" wind; it is most prevalent in undisturbed, quiet-time conditions. Generally, the fast wind is much less variable than the slow wind in terms of its speed, density, and temperature, which are relatively fixed, characterizing a solar phenomenon one can confidently call the "fast wind," whereas what is called the slow wind is highly variable in these parameters and might more aptly be called the "slow variable wind."

During solar minimum, both winds are characteristic of distinct regions of origin.

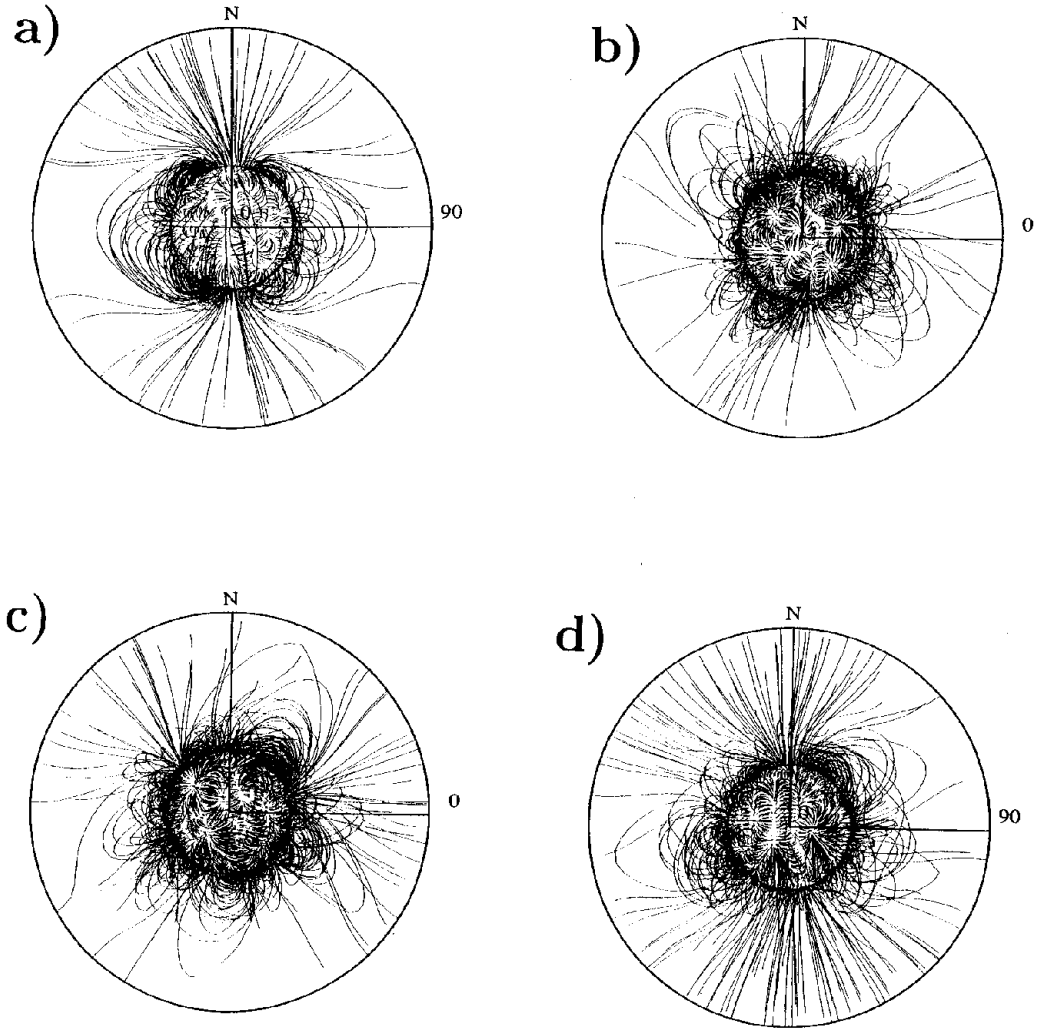

Figure 1.2 Magnetic field configurations: a) near minimum , b) the ascending phase, c) near maximum, and d) the descending phase. The solar wind configuration can be deduced quite simply: fast wind flows along open field lines, while the slower variable wind extends from the convoluted, closed field-line regions.

(Image credit: Forsyth [1999])

(See Figure 1.2a.) The fast wind is associated with coronal holes and open field regions of the corona (regions in which the magnetic field lines extend into the solar system rather than reconnecting with the surface of the sun), often originating in the Sun's polar regions. Alternatively, slow winds generally stem from the active regions concentrated near the magnetic equator (which is tilted with respect to the rotation axis, a fact that will become important in the discussion of CIRs), usually within what is called the streamer belt.

Generally, two dynamic features dictate the large-scale structure of the solar wind: coronal mass ejections and corotating interaction regions. This thesis examines the latter and its effects on the open-closed boundary (OCB) of the Earth's magnetosphere.

1.2 Corotating Interaction Regions and the Magnetosphere

One might suspect that, since the slow winds generally originate close to the magnetic equator while the fast winds often originate higher up in the polar regions, these winds go about their own trajectories, in their own domains of existence during quiet time. This segregation would be true if the magnetic axis was aligned with the rotation axis of the Sun—but that isn't the case (see Figure 1.3).

The Sun's magnetic axis makes an angle with its axis of rotation, which means as the Sun rotates, a range of magnetic latitudes intersect the ecliptic plane. Thus, if the source regions of the fast and slow solar wind endure multiple solar rotations, a succession of fast and slow solar winds will encounter Earth. Unlike wind in our atmosphere, in which a fast wind catching up to a slower wind could mix with the slower

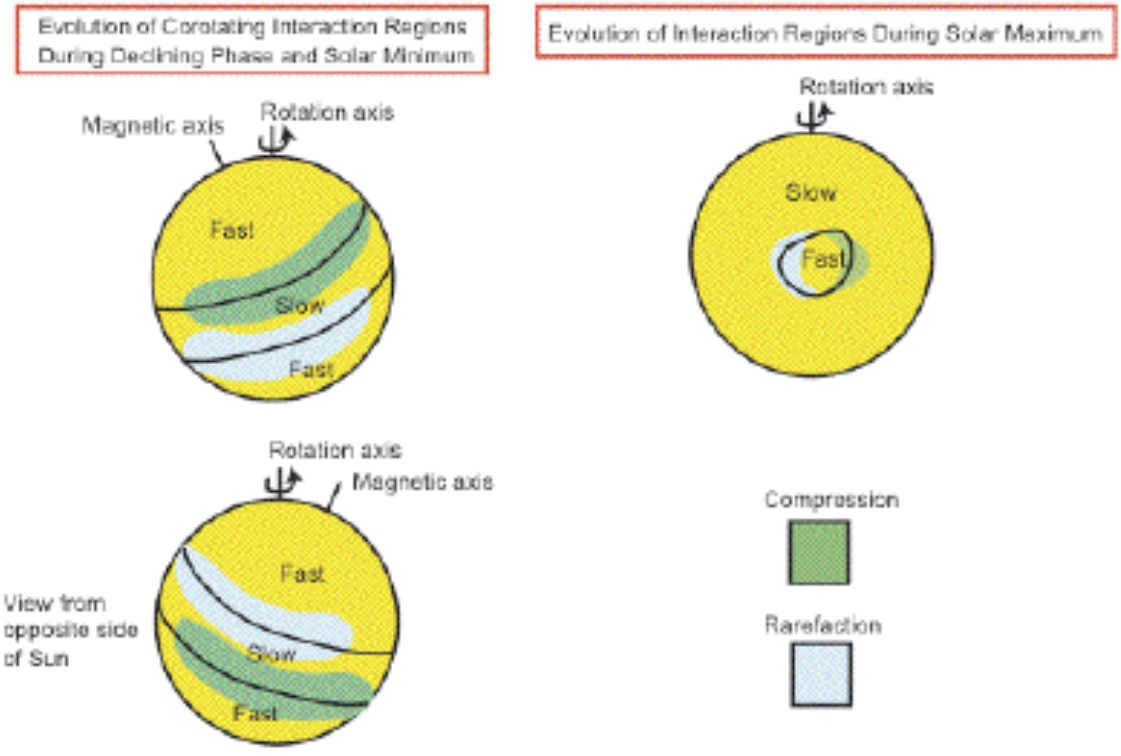

Figure 1.3 During solar minimum, the sun has a relatively simple configuration with coronal holes existing principally at high magnetic latitudes; in this case the fast and slow winds are produced in distinct domains. During solar maximum, the configuration is much more complex with production of both winds identically distributed.

(Image credit: Riley [2006])

wind while displacing it, the fast solar wind cannot penetrate into a region of slow wind; this produces an interaction region between the two winds—an area of compressed plasma and magnetic field, which when encountering Earth can trigger a geomagnetic storm (up to a few days worth of disturbed geomagnetic activity).

The compression region formed by the interaction of the two winds is fixed as the winds propagate further out into the solar system. If the source regions on the Sun persist through multiple rotations, the compression region throughout interplanetary space takes on a shape that appears to spiral about the Sun, as if the Sun is dragging the region around as it rotates about its axis. Note, however, that nothing is physically being dragged (a parcel of solar wind itself travels, to a good approximation, radially outward). This spiraling effect, which appears to corotate with the Sun, is a result of the conservation of angular momentum. This phenomenon—a region of interaction between a fast and a slow wind, which globally appears to co-rotate with the Sun—is known as a corotating interaction region (CIR). The geomagnetic storms triggered by these interaction regions tend to recur with a 27-day periodicity, in accord with the Sun's synodic rotational period. (Note that, as Riley [2007] points out, the rarefaction region shown in Figure 1.4 is also a corotating structure and is technically a region of interaction between the two winds, however it is not generally referred to as a CIR).

Figure 1.5 depicts the global aspects of a CIR. A well-known property of CIRs is that they become increasingly more dramatic at large heliospheric distances. For example, forward/reverse shock waves usually do not result until about 2-4 AU, which is beyond the scope of this thesis, but interesting to note nonetheless.

At approximately 1 AU, along the Sun-Earth axis, a CIR collides with the Earth's

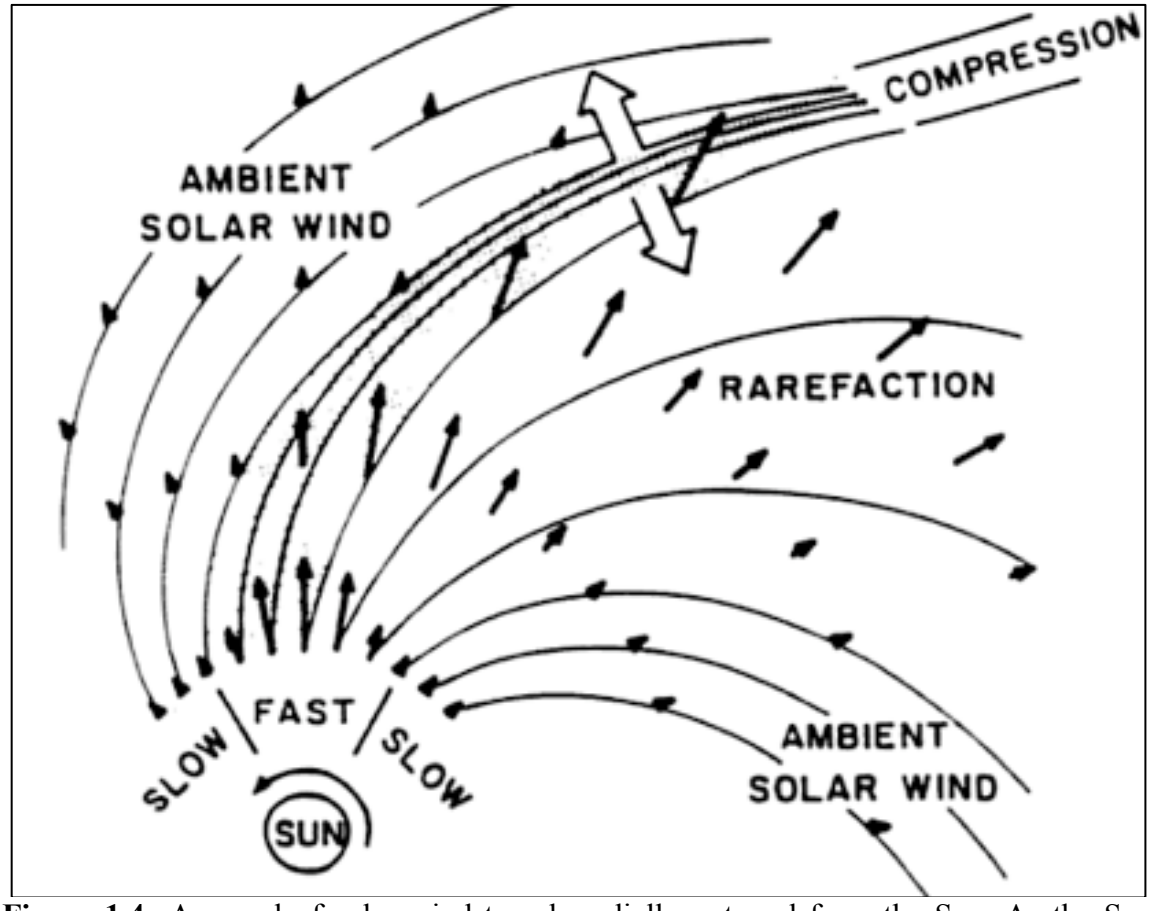

Figure 1.4 A parcel of solar wind travels radially outward from the Sun. As the Sun rotates in this picture, fast wind parcels catch up to the slow parcels released prior. The compression region that is formed appears to corotate with the Sun, although no parcel that comprises it actually is.

(Image credit: Gosling and Pizzo [1998].)

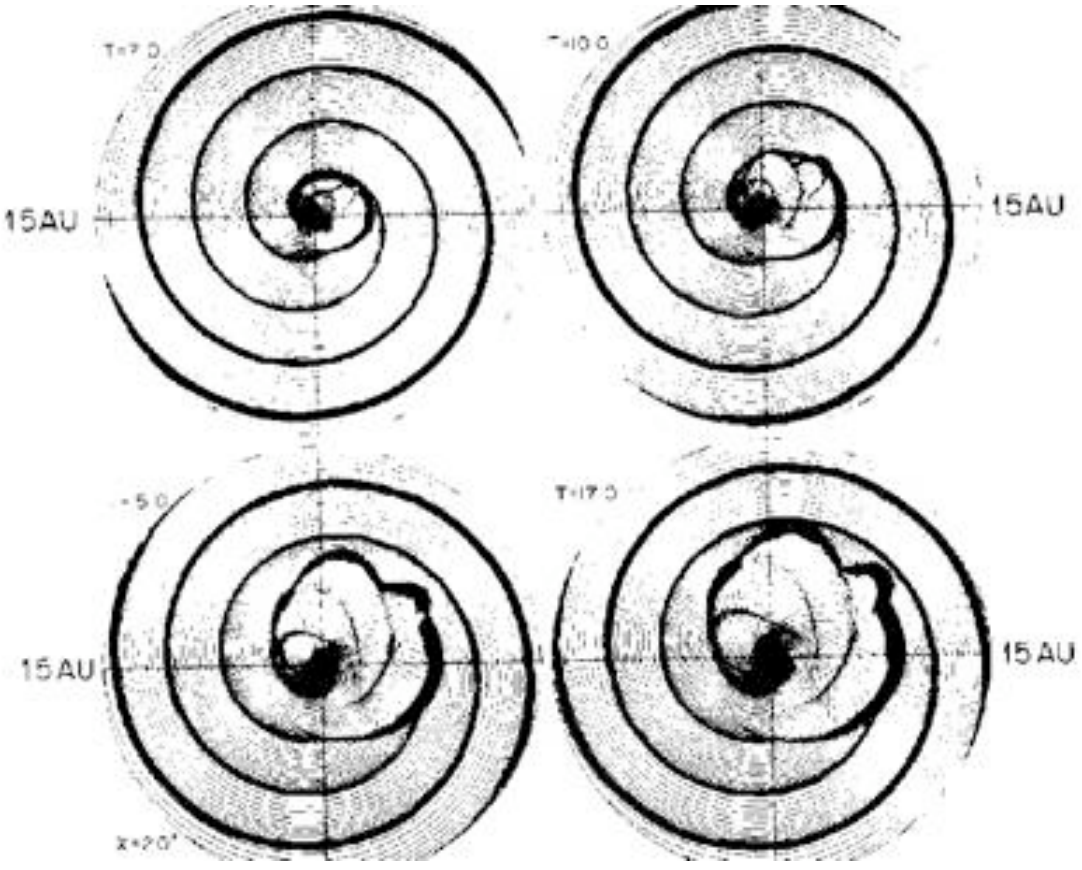

Figure 1.5 The global structure of a CIR. 1 AU = 149598000 km
(Image credit: Akasofu and Hakamada, 1983)

magnetosphere. To understand what the possible dynamics of this collision might be, one must understand the complexity and large-scale features of Earth's magnetic field.

It is well known that the magnetic field close to the Earth's surface is approximately dipolar—this was first calculated and described mathematically by C. F. Gauss using what is now known as spherical harmonic analysis in the early 19th century. Furthermore, the near-Earth field varies extremely slowly over time—on scales of years to hundreds of years. This combination renders it relatively straightforward to investigate, especially in contrast to the magnetic fields found at and above 90 km altitude, which no longer can be approximated so simply.

Ninety kilometers altitude marks the lower limit of the ionosphere: a region of ionized particles, electrons, and neutral atoms. The ionized population is due to ultraviolet radiation from the sun striking ambient atoms and molecules. At the lowest ionospheric altitudes, ionized particles are short-lived and quickly recombine to form neutrals, but ascending higher, ionization gradually outperforms recombination. At the outer limits of the ionosphere, the neutral wind component fades completely from existence; this region, dominated only by plasma, is called the magnetosphere—a realm endowed with a complex system of electrical currents formed as a result of the interaction between the solar wind and Earth's magnetic field.

Before 1959, the word magnetosphere did not yet exist. It was Thomas Gold, an Austrian astrophysicist, who coined the term in his paper "Motions in the Magnetosphere of the Earth."

The magnetosphere is formed as a result of the interaction between the solar wind and Earth's magnetic field. Although near the Earth's surface, the geomagnetic field

approximates a dipole field, this isn't the case for the large-scale structure of the field, particularly in the magnetosphere. For example, in a truly dipolar field, each field line extending from the planet's surface would reconnect at its conjugate point in the opposite hemisphere. In reality, the Earth has a region at the poles that contains open field lines; these field lines are dragged by the solar wind indefinitely out into the solar system. The boundary of this region is called the open-closed boundary; the dynamic behavior of this boundary under CIR-forcing is the topic under investigation and will be further discussed in a later section.

As the solar wind, traveling at 400-800 km/s, collides with the magnetosphere, a dynamic pressure is created on the dayside. The region where the dynamic pressure is counterbalanced by the magnetic pressure of Earth's magnetic field at ~10 R_E is called the dayside magnetopause. The currents that are created at this boundary cancel Earth's field exterior to it and reinforce the dipolar field in the interior.

As the solar wind comes in contact with the terrestrial field on the dayside, most of the charged particles in the solar wind are deflected around the earth—this deflection initializes at the "bow shock" (see Figure 1.5) and is akin to water rushing by a speedboat. This bow shock can loosely be interpreted as the point of contact between the solar wind and the magnetosphere, although it is actually not a point of contact at all: the bow shock, unlike shocks formed in more familiar media, is collisionless.

While much of the solar wind is deflected at the bow shock, it is not entirely prevented from entering the magnetosphere: a number of particles manage to funnel through magnetosphere near the poles in hole-like structures called the polar cusps. This solar wind plasma then mixes into the plasma of the magnetosphere and ionosphere,

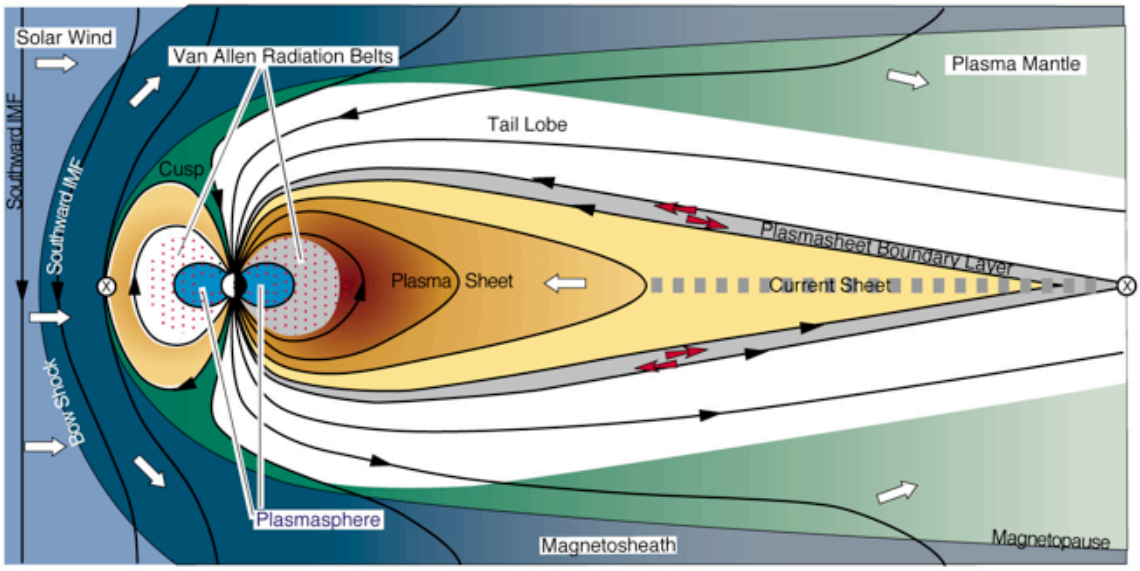

Figure 1.6 The solar wind, flowing from the left, impinges upon the magnetosphere; the embedded (southward) IMF couples with the field lines of the magnetosphere, transferring plasma through the cusps.

(Image credit: T. W. Hill)

creating the aurora.

On the nightside, the terrestrial field is elongated: this is the effect of the solar wind traversing along the exterior of the boundary separating the two plasma domains (the magnetopause), stretching and dragging the terrestrial field lines. This continual flow casts the nightside magnetosphere into a teardrop-like shape called the "magnetotail."

Solar wind energy is transmitted into the magnetosphere through a process called magnetic reconnection. This process occurs when the interplanetary magnetic field (IMF), flowing in tandem with the solar wind, couples to the dayside magnetosphere, transferring energy and momentum into the magnetosphere-ionosphere system. Reconnection is highly dependent the Bz component (in GSM coordinates) of the IMF. Namely, a high magnetic reconnection rate is associated with a strong southward component.

When a CIR crosses paths with the magnetopause, Alfvenic structures in the solar wind cause the magnetosphere to undergo vigorous oscillations and deformations—magnetic field lines in the tail bend and stretch, excessively so, such that they snap, releasing all kinds of particles and radiation into the inner-magnetosphere and ionosphere, mostly concentrating in the auroral zone. This release of energy and its associated magnetic disturbance is known as a magnetospheric substorm.

There exist three phases of a typical substorm: growth, expansion, and recovery. During the growth phase, energy from the solar wind is stored in the magnetotail. The expansion phase begins when the magnetotail becomes unstable; this is usually called the "substorm onset" and it is the point at which the accumulated energy is impulsively released. The recovery phase marks the return towards the pre-substorm state—not

necessarily geomagnetic quiet given that many substorms occur at some point in much larger and longer-lived geomagnetic disturbances called magnetic storms. Note though that despite the name "substorm," a substorm needn't take place during or be associated with a magnetic storm. The index typically used to monitor substorm activity is called the Auroral Electrojet (AE) index; these indices are derived from the magnetic-north component of the geomagnetic field at 12 reference stations situated under the auroral oval's statistical location.

A typical CIR can induce many substorms, one after another, and most CIRs ultimately conjure up weak-to-moderate geomagnetic storms; some argue that this is precisely what a geomagnetic storm is—a succession of substorms, regardless of origin—but this is still a widely debated issue (i.e. some argue that there exist evidence suggesting geomagnetic storm activity in absence of substorm activity).

In general, a geomagnetic storm has three phases: initial, main, and recovery. The initial phase of a storm can last anywhere from minutes to hours; during this phase, the horizontal component of the field increases, reaching up to a few tens of nanotesla higher than geomagnetic quiet. During the next phase of the storm, called the main phase, a sharp drop in the horizontal component is recorded, with values reaching as low as a 100 nanotesla or more below the quiet-time value; this phase can last between a half hour to several hours. The recovery phase is last phase of the storm and is the period in which the geomagnetic field gradually returns—over a day or two, up to a week—to the quiet (undisturbed) value.

It should be noted that the phase profiles of geomagnetic storms slightly differ during solar minimum conditions than those of solar maximum; this is due to origin.

During the declining phase, CIRs and high-speed streams dominate the solar wind, while structures like CMEs are scarce. In contrast, near solar maximum, CMEs and the slow variable wind dominate. Effectively, dissimilar sources generate distinct storm profiles; a CIR-generated storm, for example, usually has a more gradual onset than that of a CME-generated storm.

Common indices used to monitor storm activity are the Dst index and the Kp index. The Dst index is often used as a measure of the strength of the ring current, while the Kp index is a measure of the overall planetary disturbance and often used as a measure of magnetospheric activity. To construct the Dst index, a network of magnetograms at equatorial latitudes are used to measure the storm-time disturbance of the geomagnetic field's horizontal component every hour; a Dst value of zero represents an undisturbed field, often referred to as geomagnetic quiet time. The Kp index is a quasi-logarithmic scale with a 3-hour resolution; its values range from 0-9, where zero represents an exceptionally undisturbed magnetosphere and nine characterizes extremely severe geomagnetic storm activity, likely to destroy spacecraft, cause blackouts, and disrupt high-frequency radio transmission for up to a few days. The Kp values 0-3 are considered to represent an undisturbed field, while 4 represents a slightly upset, unsettled field; a Kp-value of 5 often corresponds with a weak geomagnetic storm; all higher values signify increasingly frenzied geomagnetic activity—moderate to severe storms.

During solar maximum (fig. 1.2c), when the solar wind is not generated in such a simple configuration as during solar minimum and the Sun is highly active with myriad explosive phenomena, it is difficult to distinguish the effects of a CIR on the magnetosphere. The simple configuration of solar minimum (fig. 1.2a) supports a study

of how corotating interaction region modulates the magnetospheric configuration and permits the possibility of distinguishing its effects on the open-closed boundary. During the summer of 2008, such quiet time existed and it was possible to single out a CIR event and to observe its effects on the OCB using a ground-based network of magnetometers distributed across the Antarctic plateau.

In graph below, one such event is recorded. Zero on the Dst axis represents geomagnetic quiet time. The initial phase clearly begins very early August 9, marked by an abrupt increase in Dst. The subsequent, quasi-discontinuous decrease in Dst marks the beginning of the main phase, and the following overall trend back to zero signifies the geomagnetic field's recovery to its undisturbed state. Notice that only at the commencement of the main phase does the Kp index reach a level associated with storm time; the sudden increase of the initial phase just barely registers as an unsettled magnetosphere. Interestingly, the magnitude of the Dst minimum (onset of main phase) is almost identical to that of the Dst maximum (initial phase), so why does the Kp index associated with these two events differ dramatically? Comparison of the Kp and Dst indices (i.e. comparison between the state of the ring current and the magnetosphere) reveals a fundamental fact about the severity of geomagnetic disturbances: an overall, highly disturbed magnetosphere (Kp index ≥ 5) is associated with a strong ring current (markedly negative Dst), which in turn is brought about by a strongly southward IMF, as previously mentioned.

Figure 1.8 displays some associated auroral activity caused by the aforementioned storm. This storm and its generators are further addressed and analyzed in later sections.

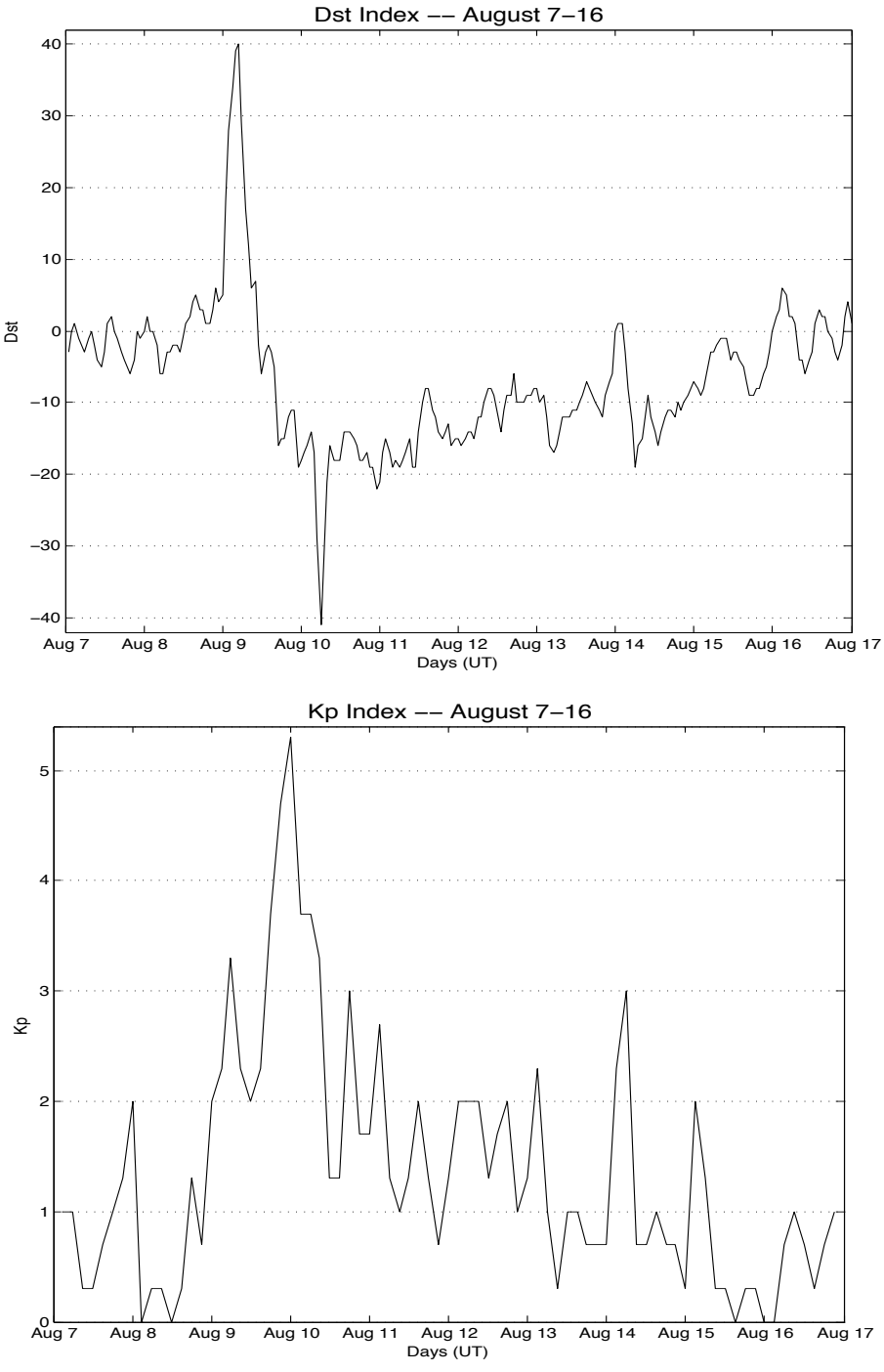

Figure 1.7 (Above) Sample Dst variation (in nanoteslas) throughout the interval August 7 – 16, 2008. (Below) Kp data for the same interval. Although Kp data is more often plotted in a box-plot format, a trace-style is used here to better compare the profiles of the two indices.

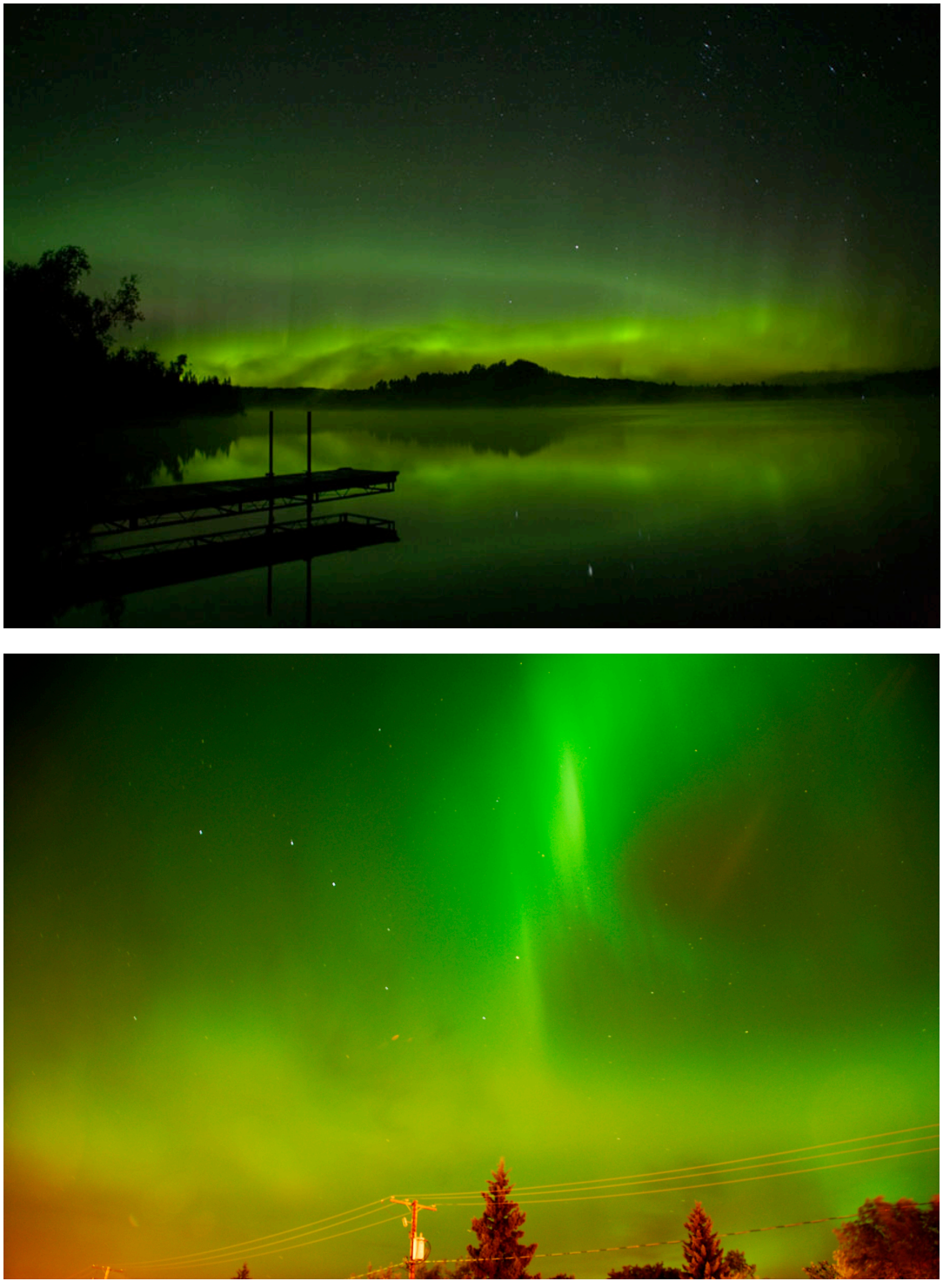

Figure 1.8 Photos of the aurora taken during the early hours (UT) of August 9, 2008. (Above) The aurora as seen by photographers John and Sallie Carlson in Lutsen, MN, USA. (Below) The aurora seen by Don J. Signori in Melfort, Seskatchewan, Canada. (Images taken from www.spaceweather.com.)

CHAPTER 2

GROUND-BASED GEOMAGNETIC OBSERVATION

2.1 The Challenges of Geomagnetic Observation

The geomagnetic field is everywhere present near the Earth's surface, but it is not everywhere accessible to observe in a rigorous and quantitative fashion without excessive interference by other sources. Power lines, cell phones, automobiles—these technological artifacts tremendously reduce the capability of observing the local geomagnetic field. Worse, in terms of a pure geomagnetic signal, are geomagnetically-induced currents (GICs) on oil and gas pipelines, long-distance communications cables, and electric power-supply grids

One might not be aware of this difficulty using an insensitive instrument such as the compass, which gives merely the overall direction of the field's horizontal component, but reveals nothing about its magnitude, gives hardly an indication of the slight dip in the field's vertical component, and is utterly incapable of detecting continuous variation of the field, which varies ever so slightly on the order of a few to a few hundred nanotesla. Being so crude an instrument, the compass cannot quite differentiate between magnetically quiet and noisy environments.

To properly observe variation in the geomagnetic field, one must implement a much more sensitive instrument, such as the fluxgate magnetometer, which can detect variations on the order of nanoteslas. An instrument with such sensitivity draws quite a different picture than the compass when attempting to observe the geomagnetic field in an urban environment. In Figure 2.1, the signal dependence of the geomagnetic field on the constituents of the local environment is shown clearly. On the upper left-hand side a

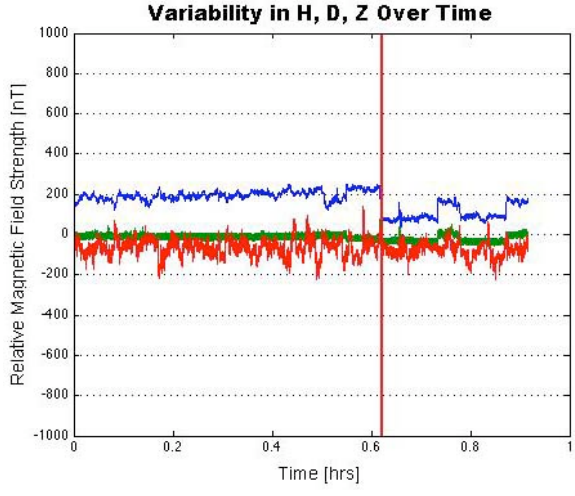

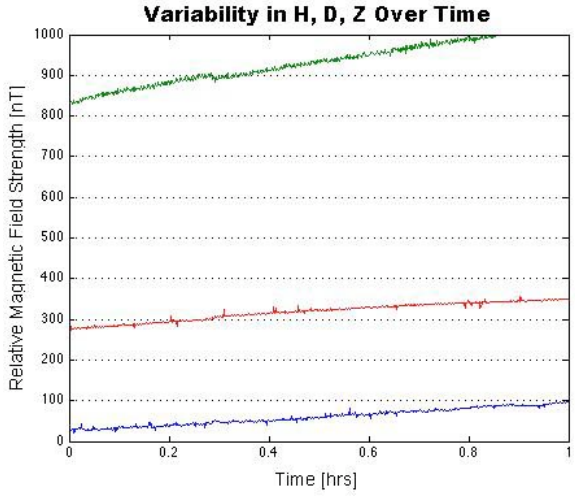

Figure 2.1 Carefully keeping track of variations in the geomagnetic field requires not only very sensitive instruments, such as the fluxgate magnetometer, but environments fairly isolated from the din of modern technologies, which are sources of magnetic noise. (Top left) a fluxgate is shown taking magnetic field measurements on the NJIT campus; (top right) the same fluxgate is shown taking measurement at Jenny Jump State Forest. The graphs below these images are samples of the respective data sets.

fluxgate magnetometer is shown on the New Jersey Institute of Technology campus in Newark, NJ, an environment strewn with the aforementioned technological elements. In comparison with data taken at Jenny Jump State Forest (the right half of Figure 2.1), it is shown that the urban environment is up to 200 times noisier, magnetically, than that of the forest. This noisiness far exceeds the level on which the Earth's field varies moment to moment, making such an environment intractable for geomagnetic field observations.

2.2 The Fluxgate Magnetometer

In this study, three-axis fluxgate magnetometers onboard the AGOs have been used to collect vectorial magnetic field data in the Antarctic.

To construct a simple fluxgate magnetometer, two ferromagnetic rods are lined up parallel to each other. The rods are each wound with an electrically conducting coil—called a primary (or "drive") coil—such that one rod is wound clockwise, the other counterclockwise. Another coil, called the secondary (or "sense") coil, is wrapped about both rods and primary coils (see Figure 2.2). An alternating current is then passed through the primary coils.

The Earth's magnetic field is faint and its intensity varies very slightly—on the order of nanoteslas. To detect these miniscule variations in such a weak field, a highly magnetically susceptible material must be employed—a material in which small variations in the ambient magnetic field produce enormous changes in the material's magnetization. The ferrite used for the rods in a fluxgate is particularly sensitive to applied magnetic fields.

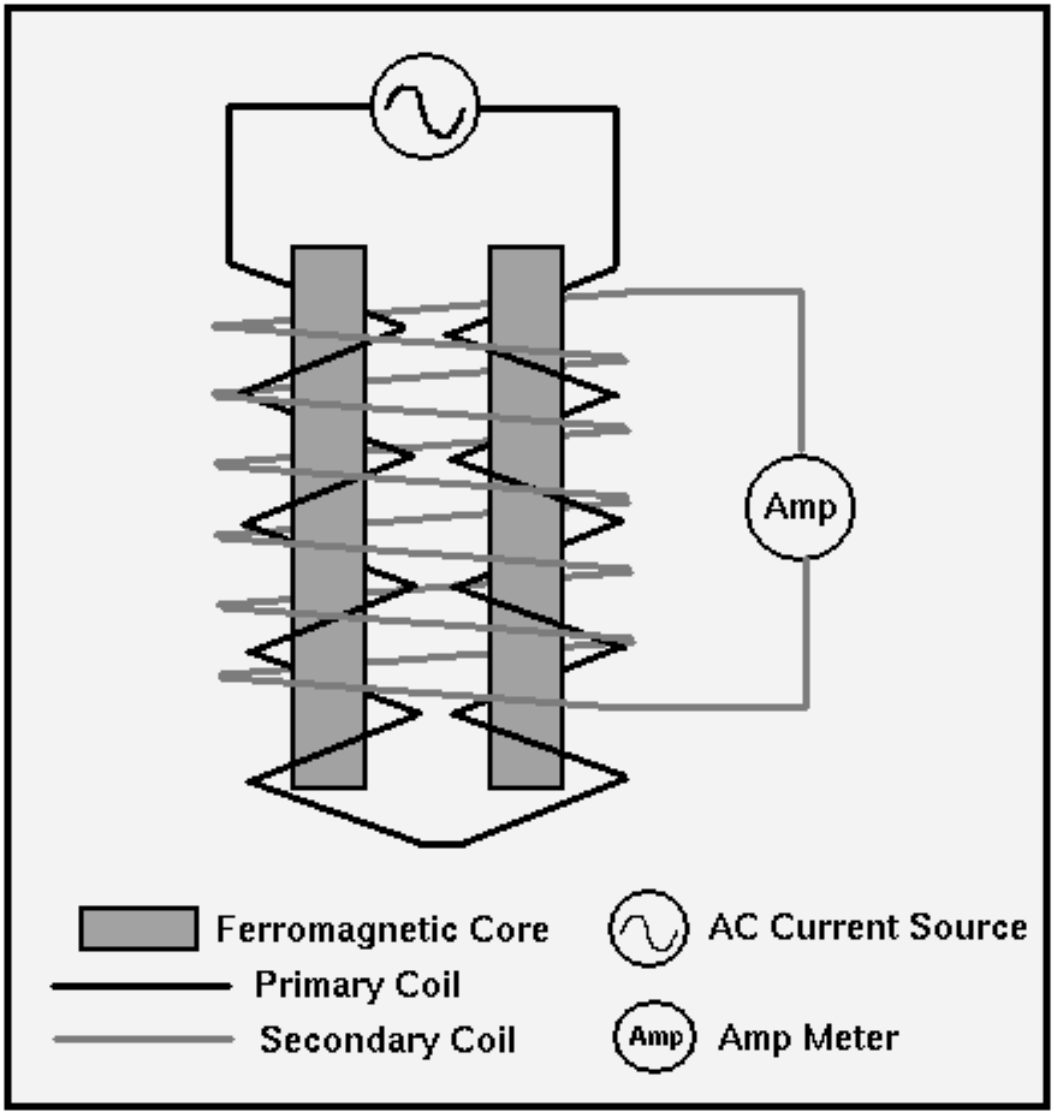

Figure 2.2 Schematic of a (single-axis) fluxgate magnetometer.
(Image Credit: Thomas M. Boyd)

When a large enough alternating current is passed through the primary coil, the ferrite goes through a cyclic saturation process: magnetized, unmagnetized, inversely magnetized, unmagnetized. Since the primary coil on one rod is wrapped in the reverse direction of the coil on the other, the induced magnetic fields of the two bars are equal in strength, but opposite in direction. Thus, in the absence of an external magnetic field, the two rods produce equal-but-oppositely-directed magnetic fields, resulting in no net magnetic flux passing through the secondary coil; the absence of magnetic flux means no current is induced on the secondary coil, which is equivalent to saying that zero magnetic field is measured. (This was to be expected since the stipulation was "in the absence of an external magnetic field.")

When measuring the geomagnetic field, the two ferromagnetic rods are predisposed to a particular magnetization without yet running an alternating current through the primary coils. If the Earth's magnetic field did not vary in time, the two rods could be aligned in the direction of the field to produce a situation such that, when running the alternating current, one rod's magnetization is favored while the other's is opposed, i.e. one rod would saturate quicker than the other and subsequently desaturate slower when the current changes direction. Since the two coils would be out of phase with each other, a measurable voltage would be measured on the secondary coil that is proportional to the strength of the externally applied field.

If the geomagnetic field varied only in strength, not direction, its variation could be recorded by continually measuring the induced voltage on the secondary coil. Since the geomagnetic field does, however, vary in both strength and direction over time, a three-axis fluxgate magnetometer is needed, which uses three of the above-described

contraptions: one is aligned with local magnetic north (called the H component), another vertically down (the Z component), and the third orthogonal to the first two (defined as magnetic east and denoted by D).

2.3 The PENGUIn-AGO Program

Antarctica provides ideal conditions for studying magnetism and the plasma interactions of Earth's magnetosphere and the solar wind, permitting scientists to paint a clearer picture of these phenomena in an environment relatively devoid of automobiles, cell phone towers, and the various other magnetically noisy artifacts imposed on an area by modern technologies.

Moreover, Antarctica provides scientists with the opportunity to observe these phenomena at high geomagnetic latitudes. Specifically, the continent renders it possible to investigate the latitudinal dependence of magnetospheric and ionospheric phenomena up to 90° geomagnetic latitude (Lanzerotti [1999]).

One does not have such luck in the north, where the high geomagnetic latitudes are predominantly occupied by open seas and floating ice in the Arctic Ocean—available land masses are foreign territories. It is impractical and politically untenable to study the polar upper atmosphere at such high geomagnetic latitudes in the north. So it is fortunate that in the south, the geomagnetic pole and the surrounding high latitude phenomena essentially lie above the sturdy ground of Antarctica, a politically neutral land mass.

The Polar Experiment Network for Geophysical Upper-atmosphere Investigations (PENGUIn) program was a direct effort to establish and maintain a network of ground-based locations at the highest of geomagnetic latitudes so that phenomena closely related

to the plasma dynamics of the dayside magnetopause and the boundary of the magnetosphere's tail could be observed firsthand. These regions are the interfaces between the solar wind (with its inherent, frozen-in magnetic field) and Earth's magnetic field and plasma environments. As harsh as Antarctica can be, it is the most practical place on Earth to observe the coupling between the two.

Before the PENGUIn program, many countries had already founded manned stations at the coastlines of the continent—but to fund and operate manned stations at much higher geomagnetic latitudes than the coast was initially deemed unviable and financially unreasonable. PENGUIn responded to this with the Automated Geophysical Observatories (AGOs), which are unmanned and can operate a full year, powered by the sun and the wind (originally, by propane-fueled thermo-electric generators), before servicing is required.

There are various instruments on board each AGO, which are kept in a room-temperature shelter. An imaging riometer is used to measure electron density changes in Earth's upper atmosphere, primarily owed to energetic electron injection from the magnetosphere. There are two types of magnetometer onboard to monitor the behavior of the local magnetic field, the fluxgate magnetometer (explained fully in next section) and the search coil magnetometer. An all-sky imager is used to monitor the aurora optically, to continuously observe the auroral morphology of the polar cap under a host of varied solar wind, IMF, and magnetospheric conditions. Each AGO is also equipped with an ELF/VLF receiver and a LF/MF/HF radio receiver. The ELF/VLF receiver is used to monitor the transport and acceleration of magnetospheric and ionospheric plasmas. The LF/MF/HF radio receiver monitors the remainder of the electromagnetic spectrum that is

Figure 2.3 An Automated Geophysical Observatory (AGO) in Antarctica. Field engineers are flown to each site about once per year and left for several days as they make various repairs and installations.

produced by processes within the magnetosphere and ionosphere not covered by the other instruments on board.

According to Rosenberg and Doolittle [1994], AGOs sites were chosen to form two arrays along carefully separated geomagnetic meridians such that temporal and spatial effects associated with polar cap observations can be distinguished and separated. One meridonal array is along the geomagnetic meridian, which includes South Pole Station and "stretches from the latitude of the polar cusp (approximately 70º geomagnetic latitude under highly disturbed conditions) to the pole of the dipole magnetic field (P6)." This array consists of sites (see Figure 2.4) P2, SP, P1, and P6 (the last of which is now defunct). The second array is positioned approximately 1.6 hours earlier in magnetic local time (MLT); it consists of the AGOs sites P3, P4, and P6. In conjunction with a few manned stations, such as McMurdo, the AGOs sites P1, P4, and P5 form a longitudinally-spaced array (at 80º magnetic latitude) that covers all 24 hours of magnetic local time.

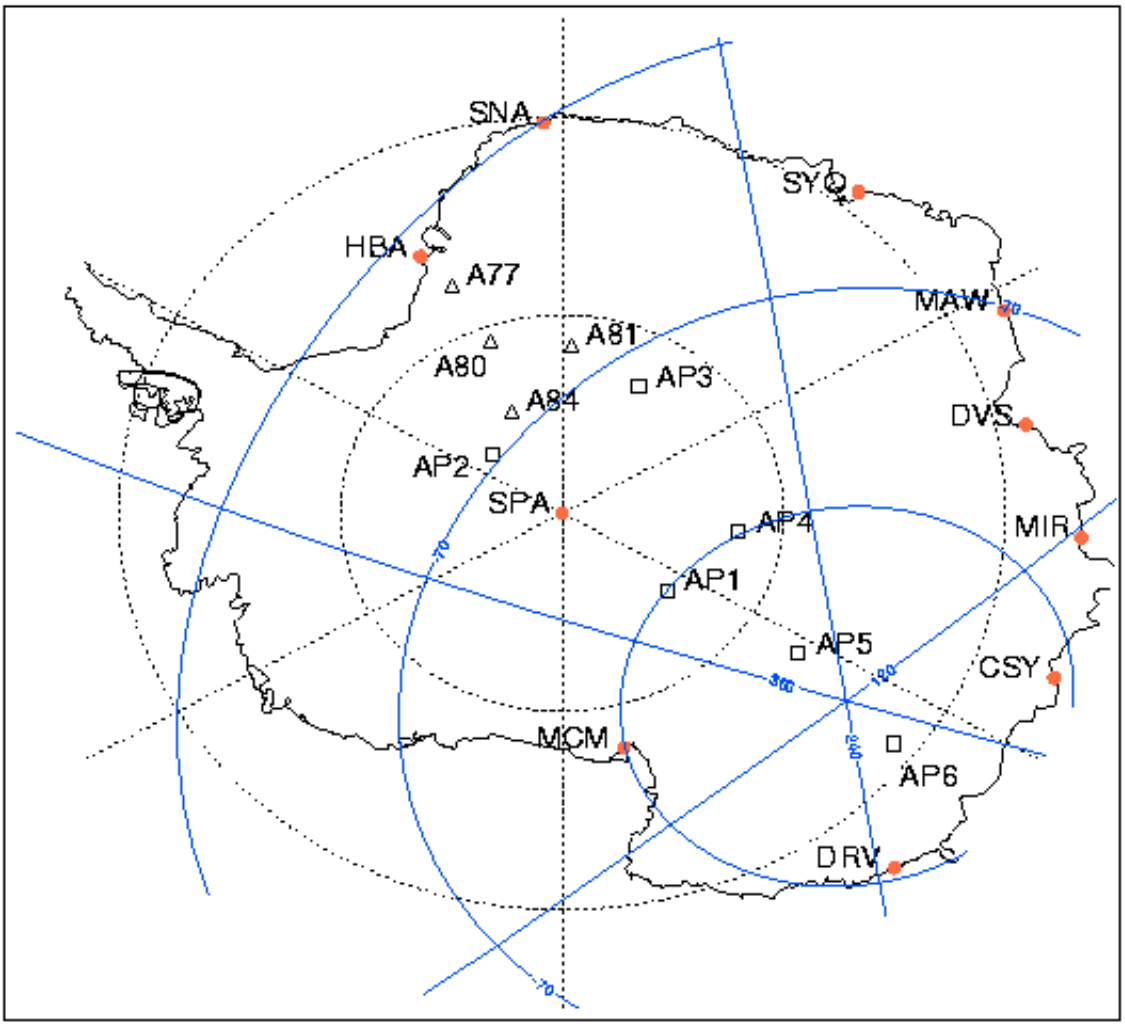

Figure 2.4 The AGOs locations; also included are various manned stations. Locations of interest are AGOs AP2 and AP3 (often denoted simply P2 and P3) and the manned stations SPA and MCM.

Table 2.1 CGM Coordinates at 100 km Altitude, as of 1997
South CGM Pole: Lat. = -74.15, Long. = 126.14

AGO	Date Established	Geographic		CGM†			
		Lat.	Lon.	Lat.	Lon.	L	UT-MLT
P1	Jan 1994	S 83.86	E 129.61	S 80.14	E 16.87	34.1	3:44
P2	Dec 1992	S 85.67	E 313.62	S 69.84	E 19.33	8.4	3:29
P3	Jan 1995	S 82.75	E 28.59	S 71.80	E 40.25	10.3	2:02
P4	Jan 1994	S 82.01	E 96.76	S 80.00	E 41.64	33.2	1:59
P5	Jan 1996	S 77.24	E 123.52	S 86.74	E 29.46	309.2	2:52
P6	Jan 1997	S 69.51	E 130.03	S 84.92	E 215.39	127.5	14:26
South Pole Station	_____	S 90.00	E 000.00	S 74.02	E 18.35	13.2	3:35
McMurdo Station	_____	S 77.85	E 166.67	S 79.94	E 326.97	32.8	6:57

† CGM: Corrected Geomagnetic Coordinates, see Glossary.

This table is based on data from: http://www.polar.umd.edu/data_archive/mag_obs.txt

CHAPTER 3

SYNOPTIC VARIABILITY OF THE OPEN-CLOSED BOUNDARY

3.1 Introduction to the Aug 9-10 Case Study

Beginning in the early hours of August 9 (UT), the AGOs network of ground-based magnetometers began recording highly disturbed geomagnetic activity (e.g. Figure 3.1). What they were recording is shown to be the effects of a collision between a corotating interaction region and the Earth's magnetosphere.

Initially, to find possible cases of CIR-interaction with the magnetosphere, Kp index data (provided by the National Geophysical Data Center) were searched for storm candidates during the days between July-September 2008, using the standard criterion that the associated time period possesses a Kp value greater than or equal to 5. Roughly 12 candidates were identified (see table 3.1), all of which are ostensibly in agreement with stream interaction regions (SIRs) observations by the STEREO spacecraft (table 3.2). Of the 12 candidates, the CIR event corresponding to Aug 9-10, 2008 was arbitrarily chosen to further investigate.

On August 6 (day 219 of 2008), at 21:17 UTC, while lagging behind Earth by 30.153º (see table 3.3), STEREO B detected a SIR. Later, on August 9, Antarctic magnetometers, the ACE spacecraft, and GOES satellites recorded the beginning of a magnetic storm (Figures 3.1, 3.3, 3.4). The disturbance observed in the geomagnetic field on August 9 correlates well with STEREO B observations of a streaming interaction region (SIR) on August 6. To see this connection, one must understand the geometry of

the duel-spacecraft STEREO mission. As illustrated in Figure 3.2, just outside Earth's orbit, STEREO B lags behind the Earth, while STEREO A precedes the Earth, just inside Earth's orbit. Given this configuration, a corotating interaction region should intercept Earth after STEREO B and before STEREO A (e.g. observe the Parker spirals in the figure).

If STEREO B's orbital speed is approximated to be that of Earth's (it's in fact a bit slower, lagging further and further behind over time), then the synodic periodicity of the Sun's rotation with respect to STEREO B is approximately 26 days. If the SIR that STEREO B detected was a corotating structure, STEREO B would have detected SIRs afterwards in multiples of 26 days. A glance at table 3.2 confirms this forecast: an SIR was detected by STEREO B on September 1 (day 245), September 28 (day 272), October 24 (day 298), and so on. Furthermore, Earth-based and near-Earth instruments should have observed an SIR within a few days of August 6, and by STEREO A some time after that.

The beginnings of a geomagnetic storm were indeed recorded by the AGOs magnetometer network (and spacecraft, as mentioned) a few days later, early on August 9 (UTC). The cause of the storm can be identified as a streaming interaction region using the data in Figure 3.3, where a sudden, dramatic increase in proton number density has been recorded by the Advanced Composition Explorer (ACE), which is in orbit at the Sun-Earth L1 libration point 240 R_E sunward of Earth. This spike in the particle population of the solar wind is characteristic of an interaction region. But is it the same SIR that was detected by STEREO B? Using 06:00 (UTC) as a contact time between the CIR and Earth's magnetosphere, the recorded commencement began approximately 57

hours (roughly 2.4 days) after STEREO B detected the SIR. Keeping with the assumption that STEREO B and the Earth share the same orbital speed, and using the fact that STEREO B was lagging behind Earth by approximately 30º, the Earth should have intercepted the SIR (30/360)*(26 days) ≈ 2.2 days after STEREO B, which is in agreement with the above estimate.

Did STEREO A observe an SIR a few days after the Earth-based observations? Leading 35.428º ahead of Earth, if one also approximates STEREO A's orbital speed to be that of Earth's, one would expect this detection to occur about (35.4/360)*(26 days) ≈ 2.6 days after the encounter with Earth. Unfortunately, the STEREO A data do not confirm this expectation (it is possible that the CIR's heliospheric latitude had increased out of STEREO A's range of detection), however the STEREO A data does show detection of an SIR at 26-day multiples, as expected, suggesting the existence of a CIR. Specifically, although there is no detection on day 225, there is detection on days 251, 276, 305, and 332. Thus, it can be asserted with confidence that the August 9-10, 2008 observations of a geomagnetic storm were—at least in part—owed to the interaction region detected previously by STEREO B and, furthermore, that this interaction region was indeed a corotating interaction region shown to persist through multiple solar rotations, fitting it neatly into the definition of a CIR furnished in chapter one.

Further analysis of STEREO and ACE data show that the geomagnetic storm recorded on August 9, 2008, was not triggered by any supplementary sources, such as interplanetary coronal mass ejections (ICMEs) or interplanetary shocks.

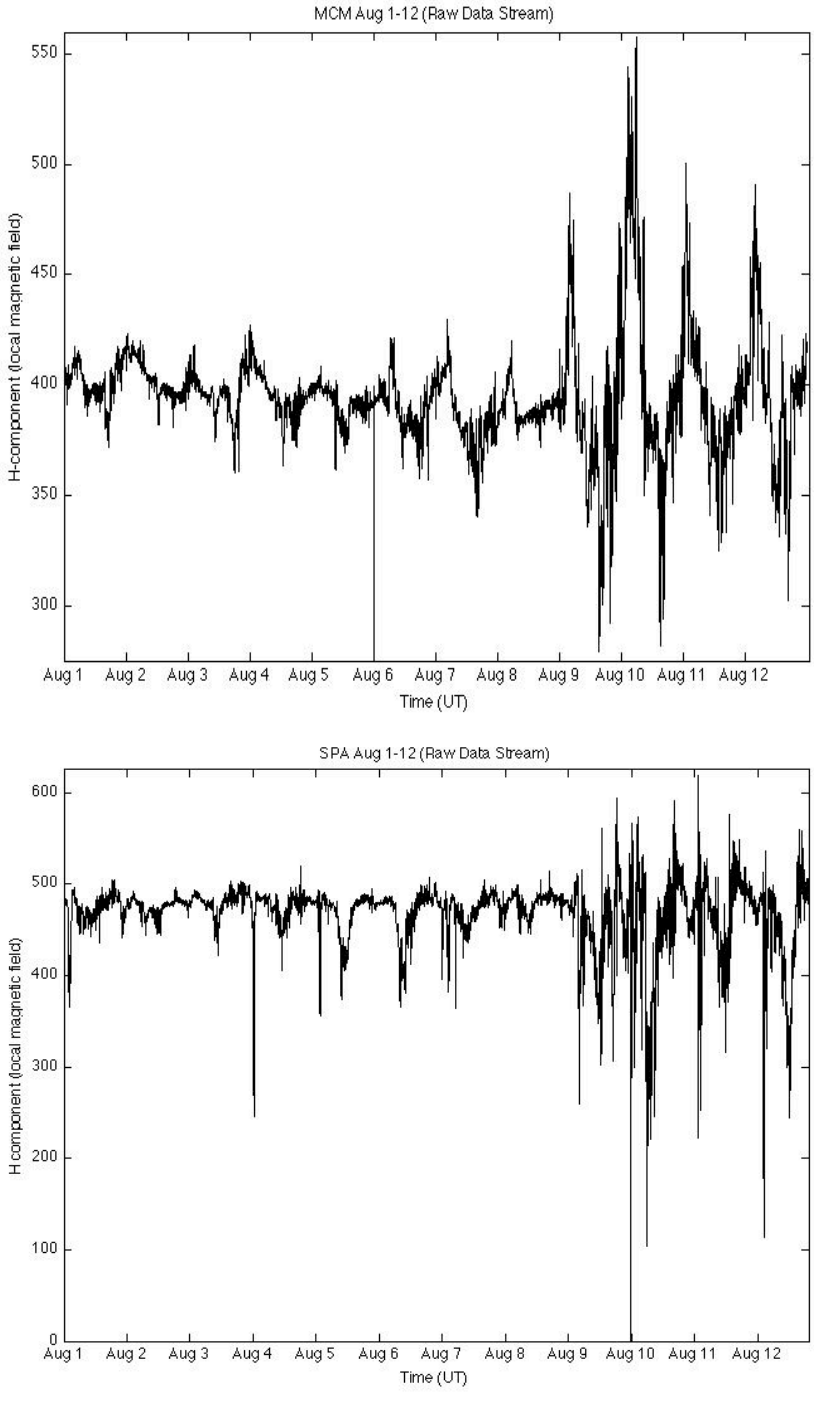

Figure 3.1 Data traces of the H-component of the geomagnetic field at McMurdo and South Pole Station.

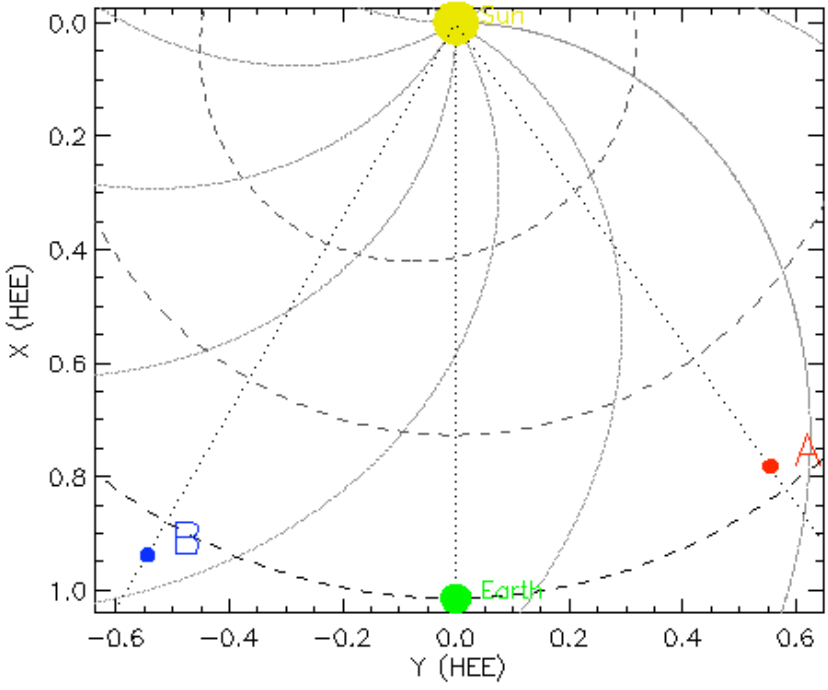

Figure 3.2 Where is STEREO? Plotted for August 6, 2008 at 21:17 UTC. Further details given in Table 3.3.

(Image Credit: http://stereo-ssc.nascom.nasa.gov/where/)

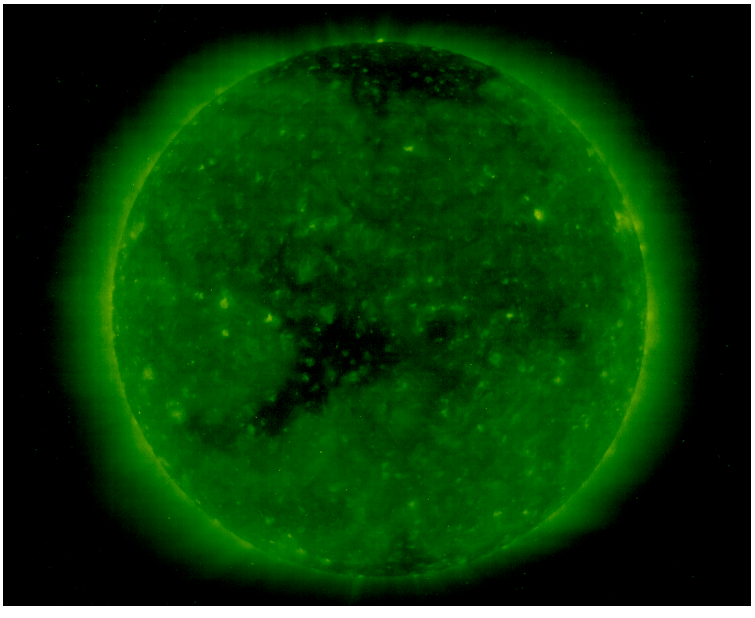

Figure 3.3 This image of the Sun was taken by SOHO's EIT instrument on August 6, 2008; during the early hours, August 9, the compression region created by the fast wind emanating from this coronal hole hit Earth.

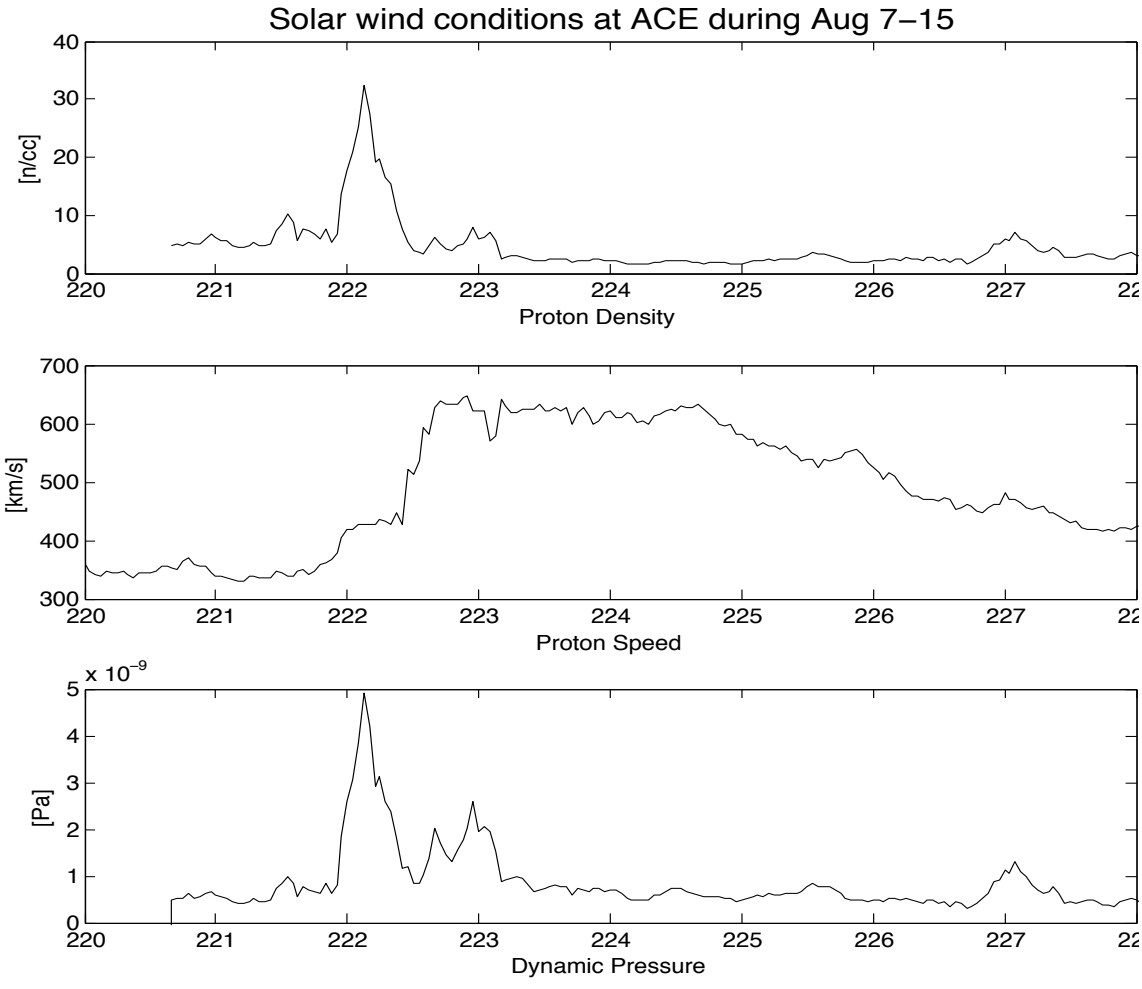

Figure 3.4 Solar wind properties between days 220 – 228 in 2008. (Top) Proton Density in particles per cubic centimeter. (Middle) The proton speed in kilometers per second. (Bottom) The dynamic pressure in Pascals.

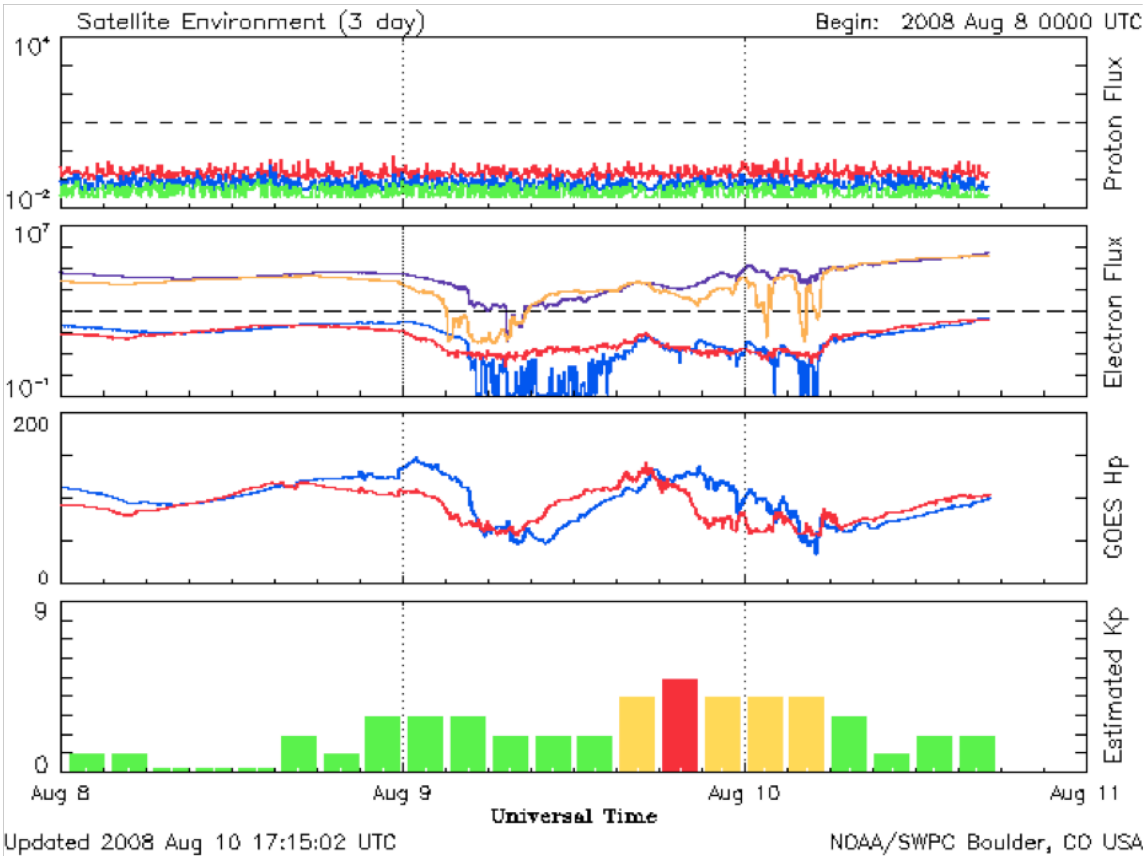

Figure 3.5 (Top) GOES 5-min averaged integral proton flux (protons/cm2-s-sr) as measured by the primary GOES satellite for energy thresholds ≥10, 50, 100 MeV. (Top-middle) This electron flux plot contains the 5-min averaged integral electron flux (electrons/cm2-s-sr) with energies ≥ 0.8, 2.0 MeV at GOES-13 (W75). (Bottom-middle) The 1-min averaged parallel component of the magnetic field in nanoTeslas (nT), as measured at GOES-13 (W75) and GOES-11 (W135). The Hp component is perpendicular to the satellite orbit plane and Hp is essentially parallel to Earth's rotation axis. (Bottom) Estimated Kp. Kp-indices ≥ 5 indicate storm-level geomagnetic activity.

Table 3.1 Observed Time Periods with Kp ≥ 5 between July and October 2008

Date	Day of Year
July 11-14	193-196
July 22-24	204-206
July 27-28	209-210
August 9-10	222-223
August 16-17	229-230
September 3-4	247-248
September 8	252
September 14-16	258-260
September 18	262
October 2-4	276-278
October 11-14	285-287
October 29-30	303-304

Table 3.2 List of Stream Interaction Regions Observed by STEREO (July-October 2008)

STEREO Spacecraft A

Start Time (doy mm/dd hh:mm)	**End Time (doy mm/dd hh:mm)**	**$^{\dagger}P_{tmax}$ time (doy mm/dd hh:mm)**	**P_{tmax} [pPa]**	**B_{max} [nT]**	**$^{\dagger\dagger}N_{pmax}$ [cm^{-3}]**	**V_{min} [km/s]**	**V_{max} [km/s]**
194 07/12 06:00	198 07/16 16:00	196 07/14 17:18	68	11.5	10	300	680
205 07/23 08:00	209 07/27 16:00	207 07/25 10:13	105	12	40	300	550
215 08/02 14:00	216 08/03 18:00	215 08/02 23:25	52	9	20	300	440
220 08/07 16:00	225 08/12 00:00	224 08/11 04:00	88	10	20	320	680
233 08/20 12:00	234 08/21 16:00	233 08/20 22:51	200	14	70	340	640
251 09/07 23:38	252 09/08 16:00	252 09/08 06:57	110	11	15	420	700
260 09/16 13:49	261 09/17 20:00	261 09/17 00:36	120	14	40	340	600
277 10/03 00:00	280 10/06 00:00	279 10/05 05:00	190	12	20	300	750
286 10/12 17:12	288 10/14 18:00	287 10/13 16:45	150	12.7	25	340	560
305 10/31 03:24	306 11/01 08:00	305 10/31 17:50	290	20	70	300	660
314 11/09 00:38	314 11/09 21:04	314 11/09 14:20	200	15.2	55	300	600
332 11/27 22:00	334 11/29 20:00	333 11/28 23:48	240	20	70	290	550
341 12/06 05:42	342 12/07 09:00	341 12/06 17:10	178	4.8	28	320	520

Table 3.2 List of Stream Interaction Regions Observed by STEREO (July-October 2008)
(Continued)

STEREO Spacecraft B

Start Time (doy mm/dd hh:mm)	End Time (doy mm/dd hh:mm)	P^{1}_{tmax} time (doy mm/dd hh:mm)	P_{tmax} [pPa]	B_{max} [nT]	N^{2}_{pmax} [cm^{-3}]	V_{min} [km/s]	V_{max} [km/s]
191 07/09 11:42	192 07/10 21:00	192 07/10 08:02	175	18.5	38	285	620
201 07/19 07:28	201 07/19 23:00	201 07/19 13:50	220	12	40	300	445
202 07/20 22:27	203 07/21 10:31	203 07/21 01:21	229	15	38	370	585
207 07/25 12:00	208 07/26 12:00	208 07/26 00:40	120	9	20	360	530
219 08/06 21:17	220 08/07 16:00	220 08/07 02:10	210	14	35	360	700
229 08/16 01:16	229 08/16 14:00	229 08/16 03:00	265.8	18	50	330	560
245 09/01 03:00	246 09/02 02:30	245 09/01 08:24	180	14	40	285	600
255 09/11 14:00	257 09/13 11:00	256 09/12 17:55	140	12.5	30	290	600
272 09/28 02:25	273 09/29 16:00	272 09/28 15:42	170	10.2	30	340	680
281 10/07 10:00	284 10/10 06:00	283 10/09 06:20	150	12	30	280	580
298 10/24 12:00	301 10/27 12:00	300 10/26 01:35	130	12	20	287	700
308 11/03 04:00	310 11/05 16:00	310 11/05 00:00	80	8	18	290	540
316 11/11 17:00	318 11/13 00:00	317 11/12 03:05	100	11.8	15	315	520
326 11/21 21:16	328 11/23 21:00	327 11/22 02:30	140	11.5	25	300	600
335 11/30 18:21	336 12/01 17:00	336 12/01 01:25	150	12.2	30	315	520
342 12/07 04:35	345 12/10 00:00	343 12/08 22:45	260	20	40	280	600
353 12/18 10:00	355 12/20 14:00	354 12/19 22:45	90	9	10	320	590

† P_{tmax} time: approximate stream interface time, because it is where the forces at the two sides are equal and in opposite directions.
†† N_{pmax}: maximum proton number density

This table is based on STEREO data from:
http://www-ssc.igpp.ucla.edu/~jlan/STEREO/Level3/STEREO_Level3_SIR.pdf

Table 3.3 STEREO Position Measurements for Aug 6, 2008

	STEREO-B	Earth	STEREO-A
Heliocentric distance (AU)	1.083646	1.014167	0.957824
Semidiameter (arcsec)	885.554	946.222	1001.883
HCI longitude	208.557	238.673	274.341
HCI latitude	3.248	6.204	7.319
Carrington longitude	281.045	311.160	346.828
Carrington rotation number	2073.219	2073.136	2073.037
Heliographic longitude	-30.116	-0.000 3	5.667
Heliographic latitude	3.248	6.204	7.319
HAE longitude	284.491	314.643	350.071
Earth Ecliptic longitude	-30.152	-0.000	35.428
Earth Ecliptic latitude	-0.233	0.000	0.087
Roll from ecliptic north	-0.400	-0.122	
Roll from solar north	-6.766	0.425	
Light travel time to Earth (min)	4.573	5.010	
Separation angle with Earth	30.153	35.428	
This table is based on STEREO data from: http://stereo-ssc.nascom.nasa.gov/where/			

Table 3.4 Partial List of Interplanetary Coronal Mass Ejections (ICMEs) Observed by STEREO A (2008)

STEREO	Start time [Year Doy Month/Day HH:MM]	End time	Ptmax [pPa]	Bmax [nT]	Vmax [km/s]	ΔV [km/s]
A	2008 187 7/5 00:48	2008 188 7/6 18:00	60	10	360	60
A	2008 248 9/4 05:25	2008 249 9/5 12:00	90	10	360	-60
See the full list: http://www-ssc.igpp.ucla.edu/~jlan/STEREO/Level3/STEREO_Level3_ICME.pdf						

Table 3.5 Partial List of Interplanetary Shocks at Stereo A (2008)

#	Year	Month	Day	Hour	Minute	Second	Forward/Reverse Shock
34	2008	7	5	0	47	53.67	F
35	2008	9	16	13	49	29	F
See the full list: http://www-ssc.igpp.ucla.edu/~jlan/STEREO/Level3/STEREO_Level3_Shock.pdf							

3.2 Multi-magnetometer Observations and Analysis

The objective of this section is to demonstrate how the open-closed boundary (OCB) can be identified and tracked using the time series magnetometer data available from multiple Antarctic stations; for illustrative purposes (and relevance), the study will focus solely on tracking the OCB during the CIR-induced storm of August 9, 2008.

Magnetometer data relevant to this study during the first half of August 2008 were available from the South Pole (SP), McMurdo Station (MCM), and AGOs locations P2 and P3 (see Figure 3.1 for sample data traces during this period; see Figure 2.4 for a map of the site locations). Three-axis fluxgate magnetometers at the AGOs sites measured the geomagnetic field at 1-second intervals, while similar fluxgates at SP and MCM executed a 10-second sampling rate; geomagnetic coordinates were implemented at all locations (that is, the field was measured in the magnetic north (H), magnetic east (D), and vertical (Z) directions); each field component has a noise level of about 0.01 nT. To create uniform data realizations, the AGOs data were binned into 10-second intervals; this helped to account for missing data realizations and repeated indexing in the initial raw data. For longer periods of missing data at any of the sites, we zero-padded the data stream.

It has previously been established (Lanzerotti [1999]) that it is possible to determine if a fluxgate magnetometer is sampling an open or closed magnetic field line by analyzing the frequency spectrum of the data stream—closed field lines, for example, characteristically exhibit disturbances propagating in the what is called the Pc5 mode, a range of frequencies with periods approximately between three and nine minutes, whereas an open field line is unlikely to exhibit this property. By identifying which

frequency modes dominate during a given time period, the local open/closed nature of the geomagnetic field at each magnetometer location was tracked before, during, and after the CIR-induced geomagnetic storm. This analysis made it possible to approximate synoptic maps of the OCB based on these observations.

For current purposes, it is not necessary to look at each field component in fine detail. Instead, the study will focus on the analysis of the H-component at each of the sites; most graphic examples are based off of SPA data, unless otherwise noted.

3.2.1 The Frequency Domain and the FFT

It is common to look at the frequency content of a continuous signal—one must only take the Fourier transform (FT). For any signal extending from negative infinity to positive infinity, the FT has perfect frequency resolution—any wave can be wholly reconstructed. But in practical cases, one doesn't have an infinite amount of time to record a signal before looking at the frequency content; the practitioner must work with a finite-length signal. In the FT's point of view, this situation is akin to multiplying the signal by a rectangle window (a function that equals one over the observation time and zero for all other times). This has undesired consequences for the frequency spectrum, since—as the adage goes—multiplication in the time domain is convolution in the frequency domain. In other words, for a finite-length signal, one does not get the frequency spectrum of the signal itself, but instead ends up with the signal's spectrum convolved with the frequency response of a rectangle function, namely the sinc function.

For example, the frequency response of a cosine function—defined for all time—is a delta function representing exactly one frequency (no surprise since a simple sinusoid

is defined by its frequency). But in practice, one's record can only be of finite-length and, thus, when Fourier transformed, the expected delta at the cosine's defining frequency is replaced by a sinc function centered about that frequency; the true frequency of the signal is found to be smeared across adjacent frequencies. This occurs because—from the transform's point of view—the signal is not a true cosine, but a cosine multiplied by a rectangle window.

This smearing out of frequency is undesirable and ought to be reduced as much as possible, but how? This question is in fact the same as asking if there is another way to "window" the time data—that is, other than using the unsolicited rectangle window. The goal is find a window whose frequency response helps to reveal the underlying spectrum that one would expect for the infinite-length signal.

In the current study, it is not a continuous-time signal being handled, but a signal sampled in uniform time steps—a discrete signal. The FT cannot handle a discrete-time signal—so it cannot be implemented to uncover the frequency content of the signal. Fortunately, there is an analogous operator that can be applied to the discrete domain. In the case of a discrete signal measured over all time, the situation could be remedied by implementing what is called the discrete time Fourier transform (DTFT). This is the analogue of the FT for discrete signals. Like the FT, the DTFT also has a continuous spectrum, albeit periodic, and has perfect frequency resolution, although only throughout the range between zero and the Nyquist frequency (half the sampling frequency); aliasing occurs for higher frequencies. The DTFT is, in fact, dual to the Fourier series; whereas the Fourier series maps continuous-time periodic signals to a discrete frequency domain,

the DTFT maps a discrete-time signals to a continuous, periodic frequency representation.

Unfortunately for frequency resolution and the privilege to access a continuous frequency spectrum, this study (and any other one) does not employ data extending from the beginning to the end of time. Like in the continuous-time scenario, a discretely sampled signal can only be recorded over a finite time length, which again is the equivalent of multiplying the signal by a rectangle window, at least from the DTFT's point of view. This multiplication in the (discrete) time domain is convolution in the frequency domain: again one will find the signal's spectrum smeared and distorted. The discontinuities at the edges of the time interval are sources of unwanted high-frequency content. Like in the continuous case, the engineer or scientist is in want of a technique that will permit him to window the time data differently than rectangularly.

The situation, though, is a touch more dire than that: for computational purposes, it is not the DTFT that is implemented, but the digital Fourier transform (DFT), which is usually implemented using the equivalent, but algorithmically more efficient fast Fourier transform (FFT). The FFT and DFT algorithms have a built-in assumption that the data set repeats itself periodically over all time:

$$\mathrm{DFT}\{\mathrm{signal}(t)\} = \mathrm{DTFT}\{\Sigma \mathrm{signal}(t-iT)*\mathrm{rect}(t-iT)\},$$

where the sum runs from negative infinity to infinity. This built-in assumption induces further spectral leakage by introducing even more discontinuities (thus unwanted high frequency content) than the rectangle window did in the DTFT case. For every period there exists a discontinuity between it and each of its neighboring doppelgangers. Yet another source of spectral leakage also comes along with the DFT: it outputs a discrete

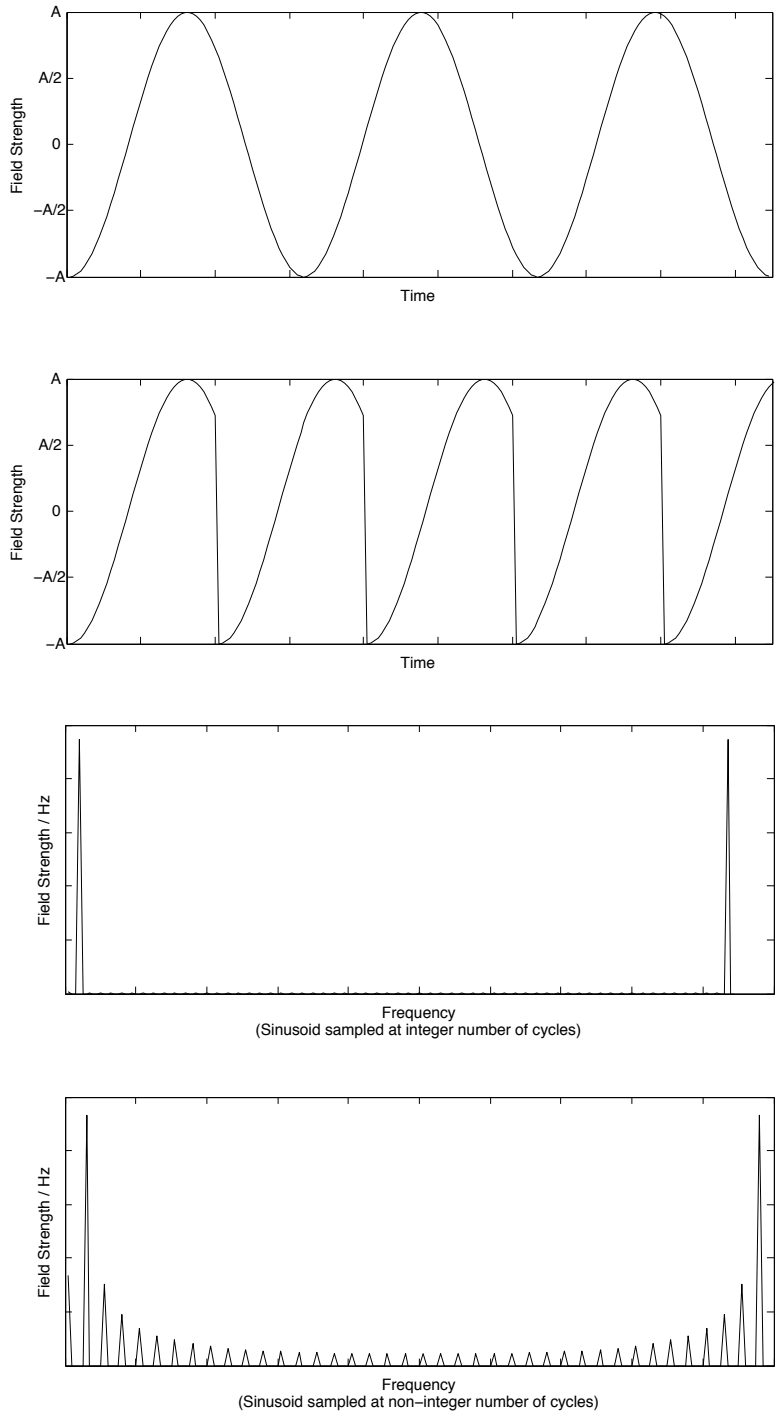

Figure 3.6 (Top) A finite length cosine signal conveniently recorded for an integer multiple of its wavelenth; the FFT assumes this signal repeats for all time and no discontinuities exist. (Top middle) A cosine wave recorded for less than a full wavelength; the FFT assumes this is one cycle of a periodic signal and thus introduces discontinuities. (Bottom middle) The frequency spectrum of the cosine signal recorded of integer number of cycles. (Bottom) Frequency spectrum for same cosine signal, only recorded for less than a full cycle; notice that the FFT-induced discontinuities wreak havoc in the frequency domain.

frequency spectrum, often called the “FFT bins.” These bins are frequencies of the form k/T_{obs}, where k is a nonnegative integer and T_{obs} is the observation time. These bins are absolutely necessary in terms of computation on a computer—they are the reason the DFT is so useful, but this utility comes at a price: a definite limit is put on the spectral resolution and, more pressing an issue, the frequency content inherent in the signal lacking wavelengths of the for k/T_{obs} must go somewhere and so are leaked into adjacent frequency bins. See the example of a finite cosine signal in Figure 3.6.

3.2.2 Windowing

To minimize the effects of spectral leakage in all the above cases (FT, DTFT, DFT, FFT), one can use a windowing function with a better frequency response. Ideally the window will weigh the data at its boundaries closer and closer to zero to remove discontinuity issues—especially important with the FFT. This is typically done using a window in which its main-lobe width is as narrow as possible and which has low side-lobes that taper off to zero. Ideally, only the frequency content of interest is addressed with minimal contribution from interfering spectral components. Unfortunately, in practice these two ideals are not always entirely independent—there usually exists a compromise between a high-resolution window and one with high dynamic range. One must make a necessary, but judicious decision when choosing which type of window to use on a data set.

The rectangle window, for example, is high resolution since its “main lobe” can be considered a delta, but it is low dynamic range since its “side lobes” are all so high (the rectangle window, being a horizontal straight line, lacks the lobes in the conventional sense of the word, thus the usage of quotations). It so happens that alternative windows

can actually introduce, overall, more spectral leakage; this at first seems counterproductive. The idea though is that these windows distribute the spectral leakage in places that do not much affect the frequency content of interest.

One of the most popular windows is the von Hann window, more often called the Hanning window; it is the window used in this study. The von Hann window has a slightly decreased resolution compared to the rectangle window, but has very low aliasing and less spectral leakage due to its lower side lobes. It is generally considered the go-to window for a wide range of applications—the rule of thumb being that if one wants to apply a smoothing window to a signal, it's almost always a safe bet to start with the von Hann window (and go from there if necessary).

3.2.3 The High-Pass Filter

It might be suggested—and rightfully so—that knowing the frequency content over all possible scales isn't necessary; this is usually the case and is dealt with using a filter, which in the discrete case is a called digital filter, but in all cases might more familiarly be known as either a low-pass, high-pass, or band-pass filter.

High-pass filtering the massaged field strength data was the first step towards a useful final product—frequencies with periods greater than two hours were stripped away by convolving the field strength time-series with the necessary filter coefficients, computed using IDL's digital filter function.

3.2.4 Processing the Magnetometer Data

After high-pass filtering the data stream, a von Hann window was applied to it; the resulting signal was then run through IDL's fast Fourier transform.

The IDL FFT algorithm is designed to give back a complex N-element array, where N is the number of data samples taken during the period of time under consideration. The useful frequencies returned by the FFT are of the form:

$$\mathrm{f(k)} = \frac{k}{N} S = \frac{k}{T_{obs}}$$

where k is the array index running from zero to N/2 (or, in terms of observation time, from zero to $\frac{T_{obs} S}{2}$) and S is the sampling rate. Indices greater than N/2 (corresponding to the Nyquist frequency) generate repeated information corresponding to the role that "negative" frequencies play in normal Fourier analysis—they are unneeded and therefore discarded. It is easily seen from the equation that as the number of samples N (a proxy for the observation time) gets bigger, one is able to resolve closely spaced frequencies better and, overall, obtain better spectral information in general (if the observation time included all time, the frequency resolution would be continuous; this is the case for the DTFT).

At the AGOs sites, the magnetometer sampling rate is 1 Hz; as previously mentioned, this data was subsequently binned, inducing a 10 Hz sampling rate. The MCM and SPA data came preprocessed in 10 Hz form. Although, the total observation time in this study encompasses several pre-storm days as well as a handful of storm-time days, knowing the frequency content of the entire interval all at once isn't very useful since one could not actively distinguish the evolution of the content before, during, and

after the CIR-forcing on the magnetosphere. To remedy this, the data set was broken into smaller, 1-hour windows; furthermore, the 1-hour windows were spaced ten minutes apart such that the frequency content of the magnetic field at each site could be monitored over time. This technique is referred to as a sliding window technique. To look at real numbers instead of the complex numbers obtained from the FFT, the power spectral densities (PSD)—also referred to as simply the power spectra—were then calculated from such a series of data sets, where

$$PSD \quad \propto \quad |\int x(t)h(t)e^{-iwt}dt\,|^2$$

In this equation, x(t) represents the data stream and h(t) a hanning window.

In its raw form (Figure 3.7a), a typical power spectrum does not lend itself to visual analysis—the frequencies being considered have power that ranges over several orders of magnitude. To work the data into a more visually pleasing form, one can plot the signal on a log axis (Figure 3.7b); in this Figure, you can easily distinguish the power of each frequency. One could go a step further and implement a log-log data plot (Figure 3.7c); in this log-log domain, the data reveals an interesting characteristic: there exists a linear feel to the power spectra when represented in this way. In fact, one will notice (Figure 3.7d) if a best-fit straight line is overlaid, the power at all frequencies varies from the linear fit in the same fashion. If, instead of using log axes, the log of the data was taken—resulting in an identical curve (see Figure 3.8a)—then one can again find the linear fit. The advantage now is that this linear fit can be subtracted from the log data, leaving what is referred to as residual PSD data. In this format, the power of each frequency is put on a similar footing, mostly varying within the interval (-2,1).

In Figure 3.8b, the data has been flipped on its side; this isn't an important step in the data analysis, but is done as a visual aid to address how the data presentation changes from that in Figure 3.8a to that in Figure 3.9; you will also notice that the frequency axis has been rehashed into a period axis—this is just a matter of preference. In the final data presentation, it is this period axis that is the y-axis, while time takes on the x-axis (see Figure 3.8c). In this format, if the residual PSD data is portrayed on a spatial axis, the data presentation would take the form of a very jagged mountainous surface—much of the important details would be lost to the eye. To remedy this, the residual PSD data are not represented spatially, but with a color axis (Figure 3.9).

3.2.5 Reflections on the Physical Meaning of the Linear Fit

It might be beneficial to stop and consider what the abovementioned linear fit might represent physically; after some reflection, one might conclude that the linear fit is representative, perhaps, of an undisturbed geomagnetic field—a theoretical equilibrium state. By subtracting this fit then, one is attempting to look only at variations of the field from this proposed equilibrium state by ignoring how or why this might be the equilibrium state. This interpretation is good enough for current purposes, but it should be pointed out that it isn't all too stringent or precise an interpretation. For one, the angle of this linear fit is subject to variations over time (what might that mean?) and, two, even during the supposed quiet-time data (observe the first 45 hours in Figure 3.9), the residual PSD hardly borders zero at all frequencies and oscillations are still present. The latter phenomenon arises because the data itself is collected as the Earth rotates, shifting the magnetometer's position relative to the—the dayside and nightside fields differ.

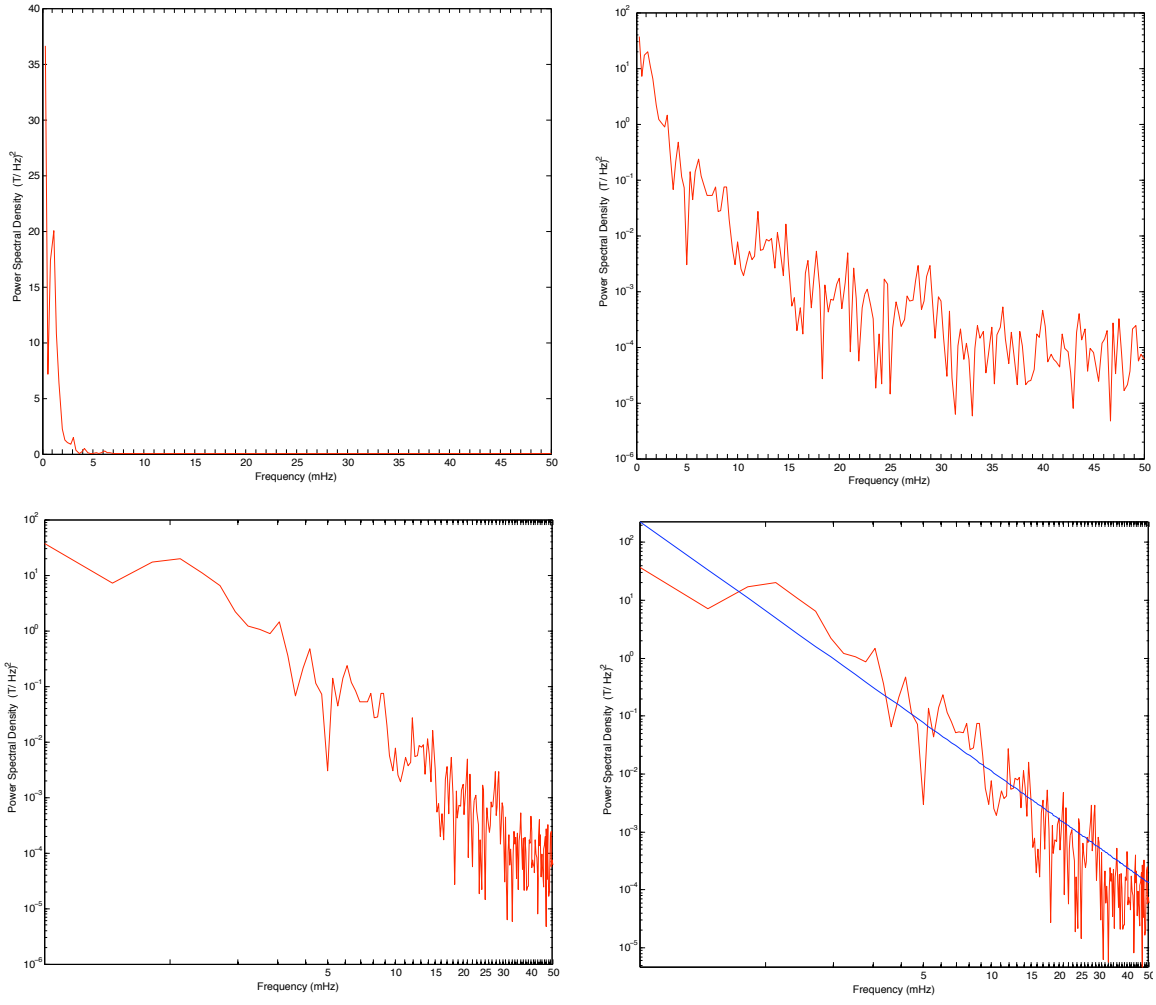

Figure 3.7 These plot examples use a data set from SPA corresponding two about two hours into August 7, 2008. (Top left) Plot of the PSD, unaltered. (Top right) plot of the PSD on a log axis. (Bottom left) Plot of the PSD in the log-log domain. (Bottom right) The log-log domain reveals a pseudo-linear relationship.

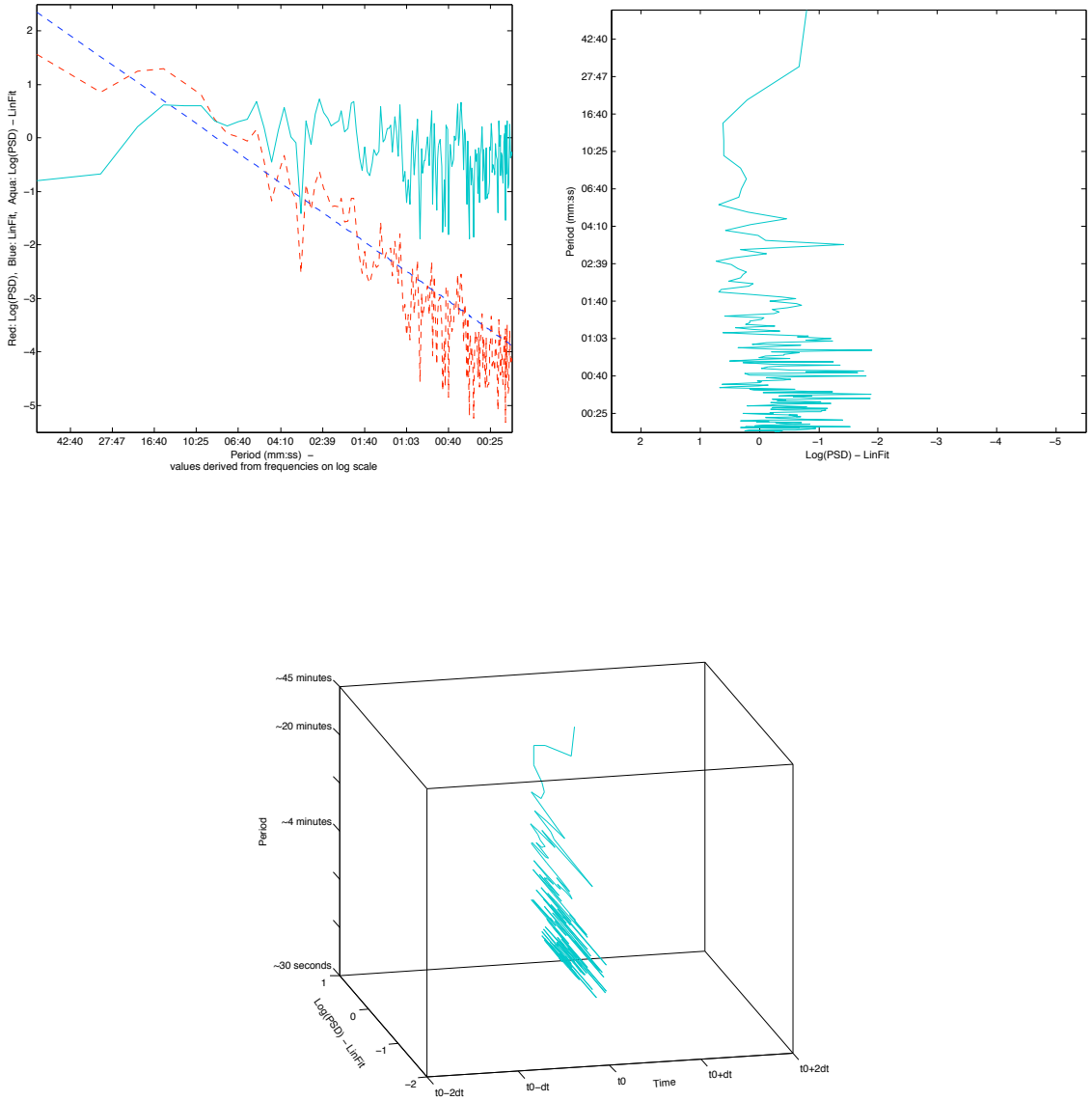

Figure 3.8 (Top left) Similar in look to the signal plotted in the log-log domain, the logarithm of the signal is plotted on a standard axis; a linear fit is found and subtracted, resulting in a "residual PSD." (Top right) In the final data presentation, the frequency (period) data is on the y-axis. (Bottom) The final data presentation will necessarily include a series of jagged curves, resulting in a visually dissatisfying mountainous surface; the solution is to plot the signal data on a color axis.

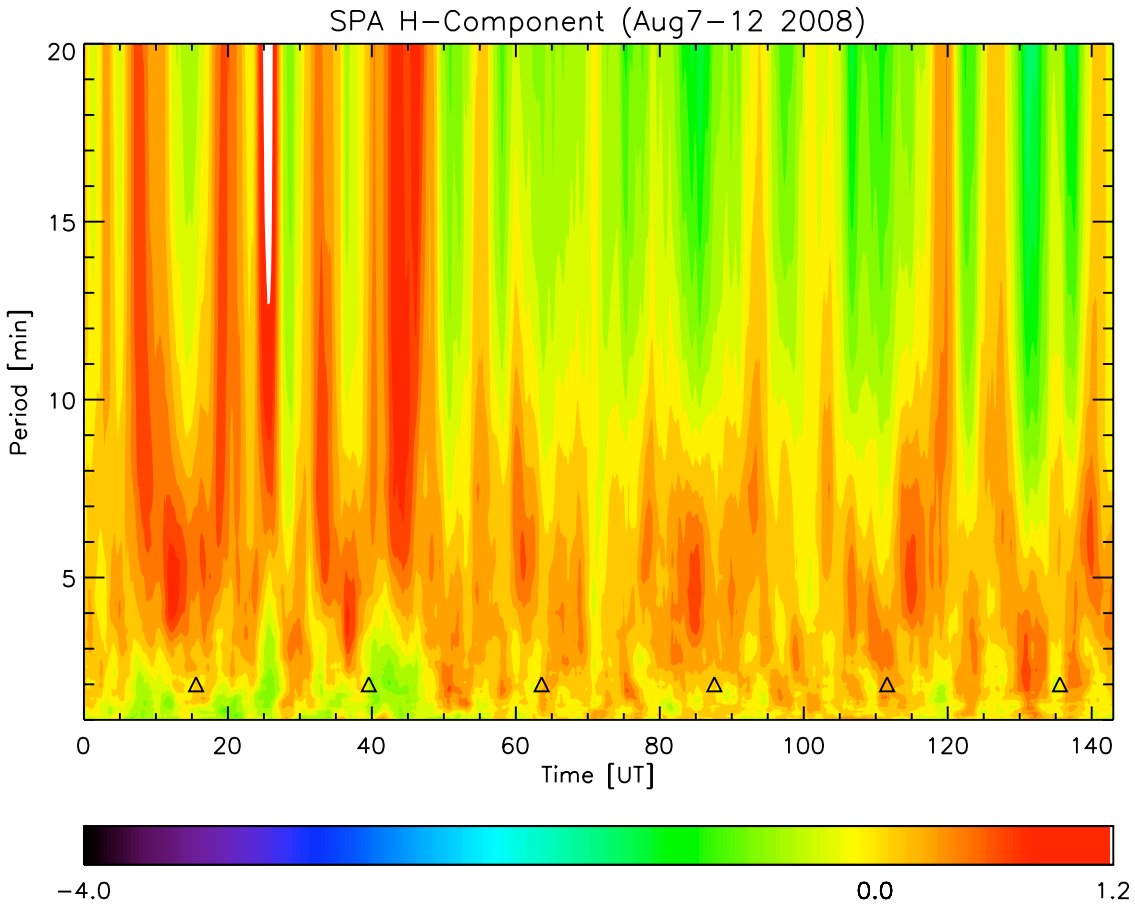

Figure 3.9 The final data presentation; the frequency data (labeled by periodicity) occupies the y-axis; the time evolution of power (technically, residual PSD) is given by changes in color.

3.2.6 Interpretation of the Data Presentation

In the residual PSD time series above (Figure 3.9), on August 9 (~50 hours) and thereafter much more power lies within frequencies having periods between three and nine minutes—this change of character marks commencement of the geomagnetic storm. The indicated frequencies are known as Pc5 modes; they are the frequencies of standing Alfven waves and indicate that a closed field line at the open-closed boundary was sampled by the fluxgate at the corresponding moment in time (Lanzerotti [1999], Lessard et al [2009]). The red columnar structures containing a host of frequencies with periods greater than 10 minutes or so indicate a field line that stretches far into the tail is being sampled. In vertical regions where Pc5 modes and the long-period modes are absent, one is sampling an open magnetic field line. (See Figure 3.10 for picture of magnetosphere.)

Data presentations covering both pre-storm and storm-time data for all relevant Antarctic locations can be found in Figures 3.11 and 3.12.

On an undisturbed day, SPA is equatorward of the OCB on the dayside and poleward of it on the nightside (i.e., the OCB passes over SPA at dawn and dusk); one should expect that the August 1-6 power spectra of SPA in Figure 3.6 demonstrate a 12-hour periodicity of short-lived Pc5 structure. Indeed, a periodic structure is observed: at about 10 hours into August 6, a high-power Pc5 event is observable; next at about 22 hours, a low-power Pc5 structure appears; again, at 35 hours is the return of the high-power formation; at about 47 hours nothing is markedly observable, but this isn't too surprising given its predecessor 24 hours previous was fairly low-power; at around 60 hours, a return of the Pc5 mode is registered; and so the pattern continues: a weak presence at 72 hours, followed by a strengthened return at 85 hours, etc. Note that once

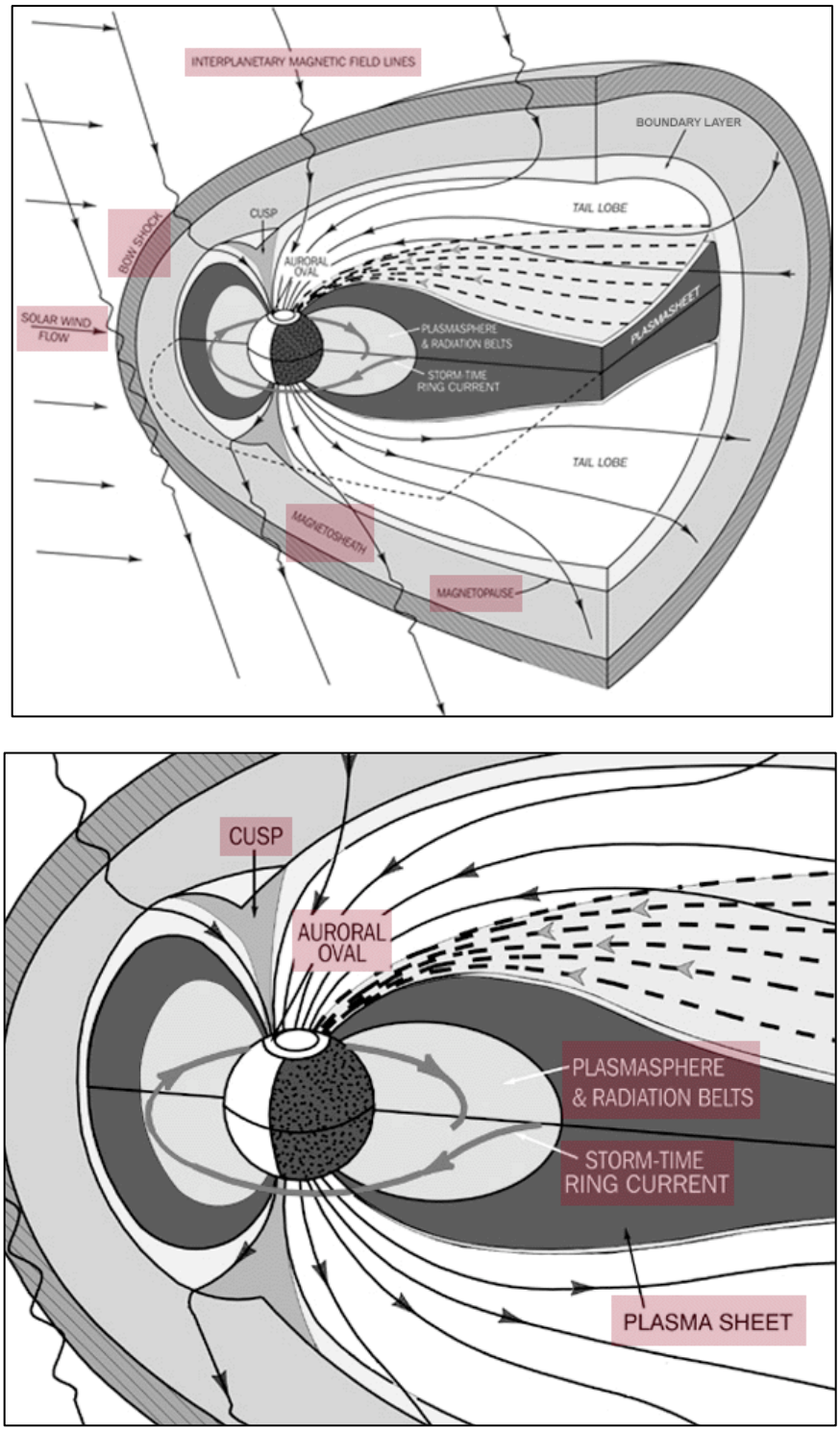

Figure 3.10 The largescale structure of the geomagnetic field; open field lines reconnect with the IMF in both sunward and antisunward directions, while closed field lines emerge from Earth's surface and return in the opposite hemisphere.

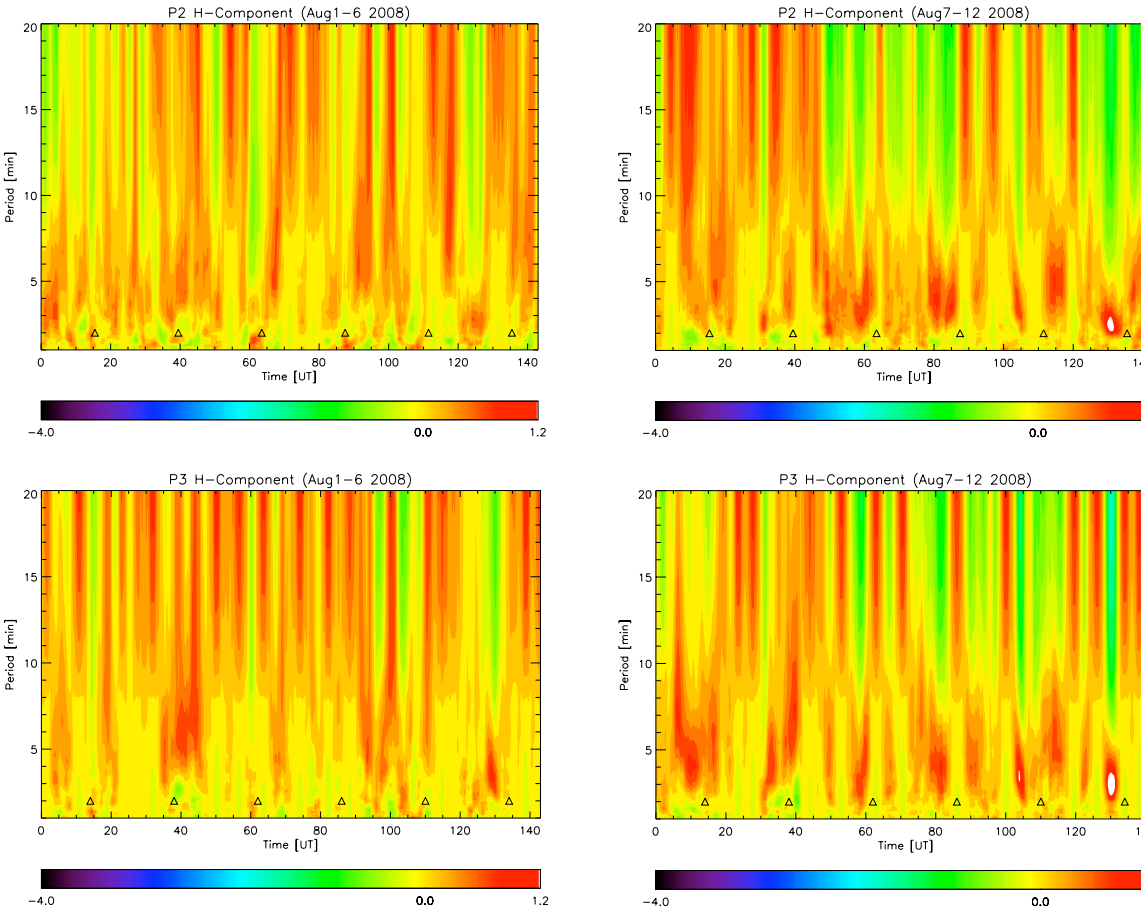

Figure 3.11 Residual PSD data throughout August 1-12 at (top row) P2 and (bottom row) P3.

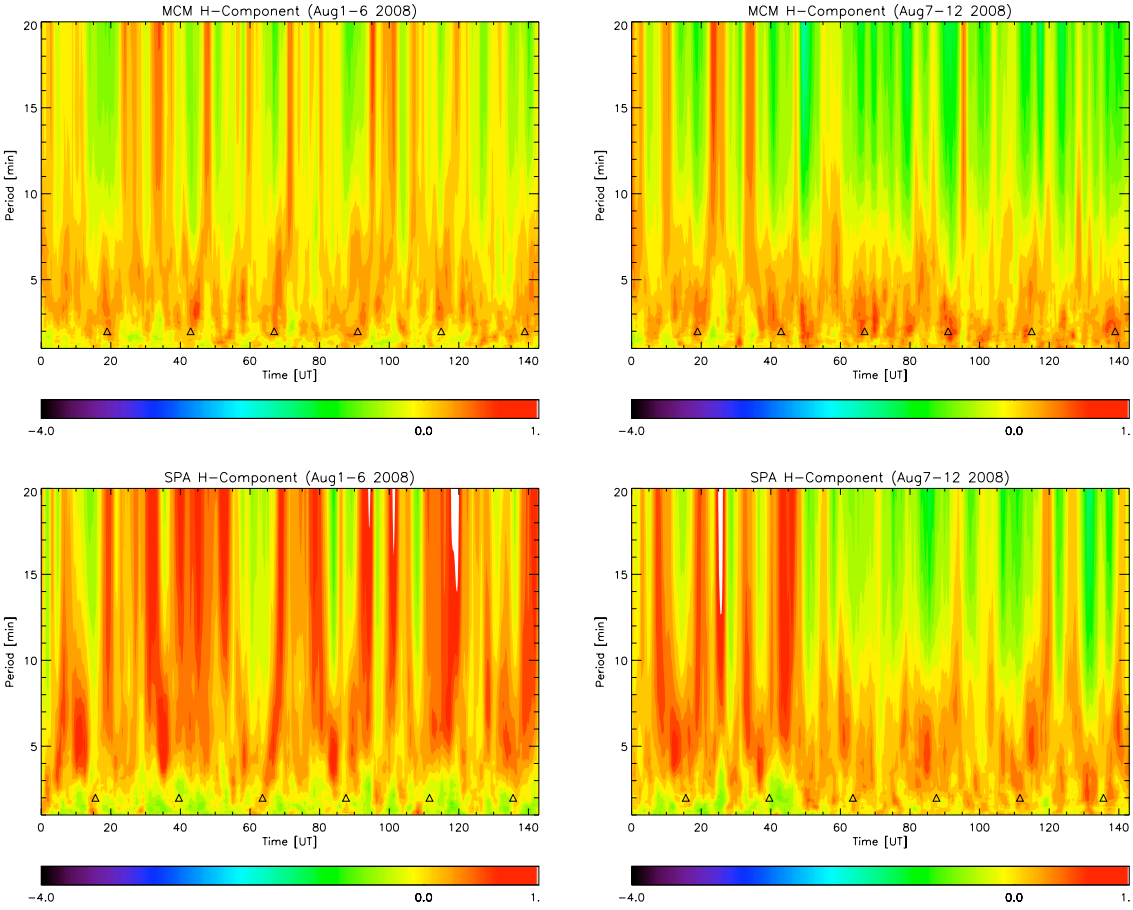

Figure 3.12 Residual PSD data throughout August 1-12 at (top row) MCM and (bottom row) SPA.

the storm begins (refer to the August 7-12 spectra presentation), tail lines become rare and there is an oscillation between closed lines at the edge of the OCB and open lines within the OCB.

In the graphs below, Figure 3.14, the data is rehashed so that one can better visualize just when an open or closed field line is being sampled. The four curves represent the relative power in a specified band at the four locations. In both graphs, the black line represents a noise floor, in which what lies below is to be considered noisy, unusable information. The noise floor was chosen such that McMurdo lacks Pc5 modes, which under most conditions ought to be the case given that McMurdo (at 80º invariant magnetic latitude) consistently lies within the OCB and, thus, should exhibit mostly open field line signatures with, perhaps, speckled hints of long-period tail lines (see MCM spectra in Figure 3.6). Note that in both graphs, the black trace corresponds to P2, the blue to P3, the green to MCM, and the red to SPA.

The top graph of Figure 3.14 represents the relative power of the long-period "tail" frequencies (defined here as frequencies with periods between 10-30 minutes); signals below the noise floor are not considered; the information lying above the noise floor represents moments in time when a field line extending into the magnetotail is being sampled by the corresponding magnetometer (may be closed or open). In the bottom graph, the relative power of Pc5 modes (taken in this plot to be frequencies with periods between 3-6 minutes) over time at the different sites is displayed; information above the noise floor represents moments when a closed field line at the leading edge of the OCB has been sampled. If both the long period frequency and the Pc5 mode are present, a closed field line extending into the tail was sampled. During instants in which a station

exhibits neither mode (when both signals lie below the noise floor), an open field line has been sampled.

As an example, look at the red traces—the relative power of the frequencies present at SPA. From about 50 hours on (that is, beginning early August 9 and throughout most of the day), it is shown that SPA goes from resting on a magnetic field line extending into the tail to an open field line. This corresponds roughly with the power spectra in Figure 3.6, given that much of power has now been attributed to geomagnetic noise.

Given this rough approximation of the dynamic behavior of the open-closed boundary, it is possible to check if these observations correspond with the predictions given by current space weather models. In particular, the Block Adaptive-Tree Solar-wind Roe-type Upstream Scheme model, developed at the University of Michigan, is put on trial.

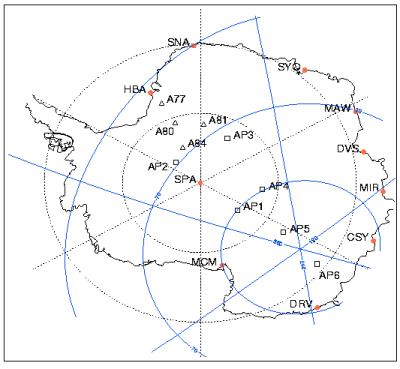

AGO	Date Established	Geographic		CGM†		Local Noon
		Lat.	Lon.	Lat.	Lon.	UT
P1	Jan 1994	S 83.86	E 129.61	S 80.14	E 16.87	15:44
P2	Dec 1992	S 85.67	E 313.62	S 69.84	E 19.33	15:29
P3	Jan 1995	S 82.75	E 28.59	S 71.80	E 40.25	14:02
P4	Jan 1994	S 82.01	E 96.76	S 80.00	E 41.64	13:59
P5	Jan 1996	S 77.24	E 123.52	S 86.74	E 29.46	2:52
P6	Jan 1997	S 69.51	E 130.03	S 84.92	E 215.39	2:26
SPA	_____	S 90.00	E 000.00	S 74.02	E 18.35	15:35
MCM	_____	S 77.85	E 166.67	S 79.94	E 326.97	18:57

Figure 3.13 AGOs locations

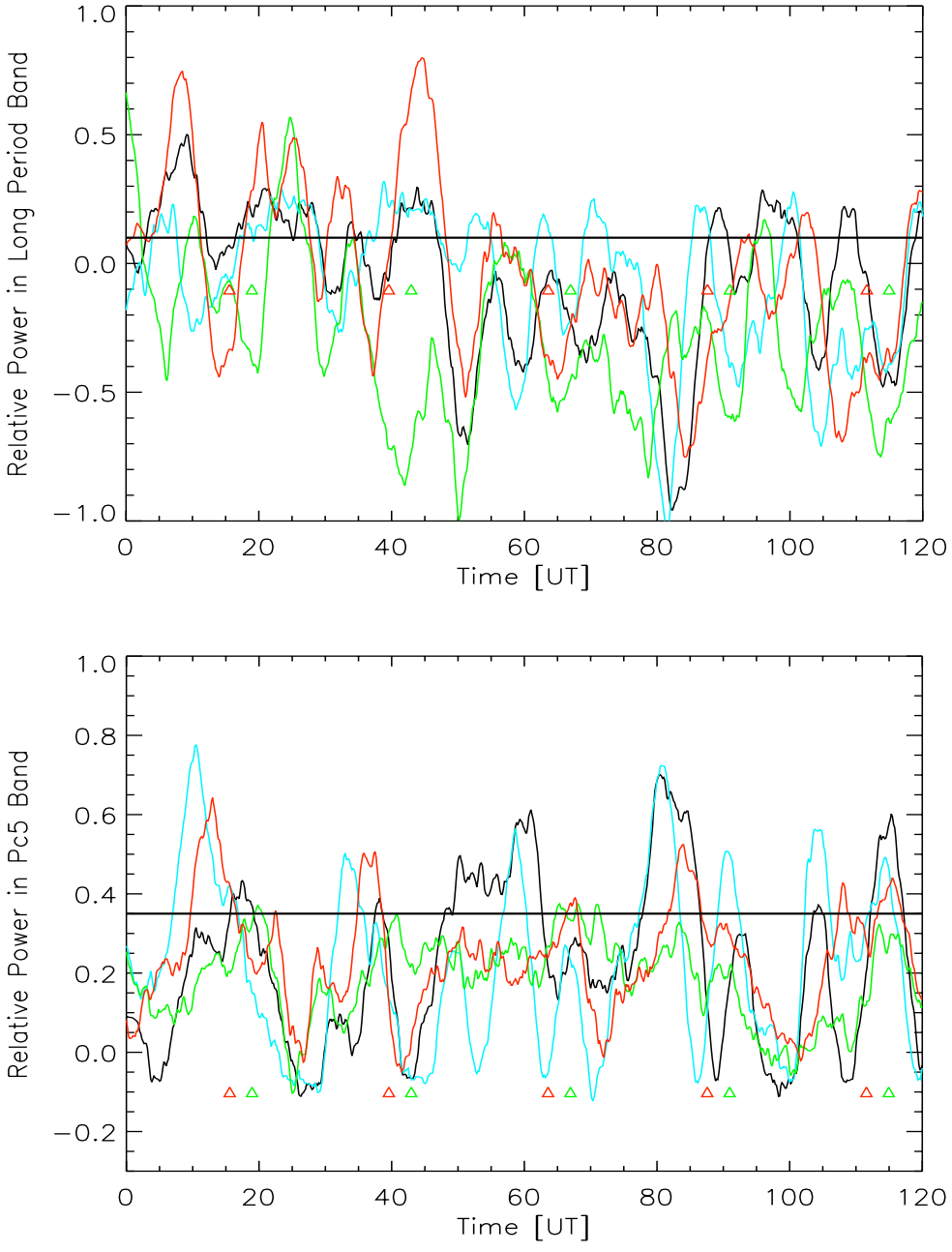

Figure 3.14 Relative power in the long-period and Pc5 bands over three days, August 7-9, 2008.

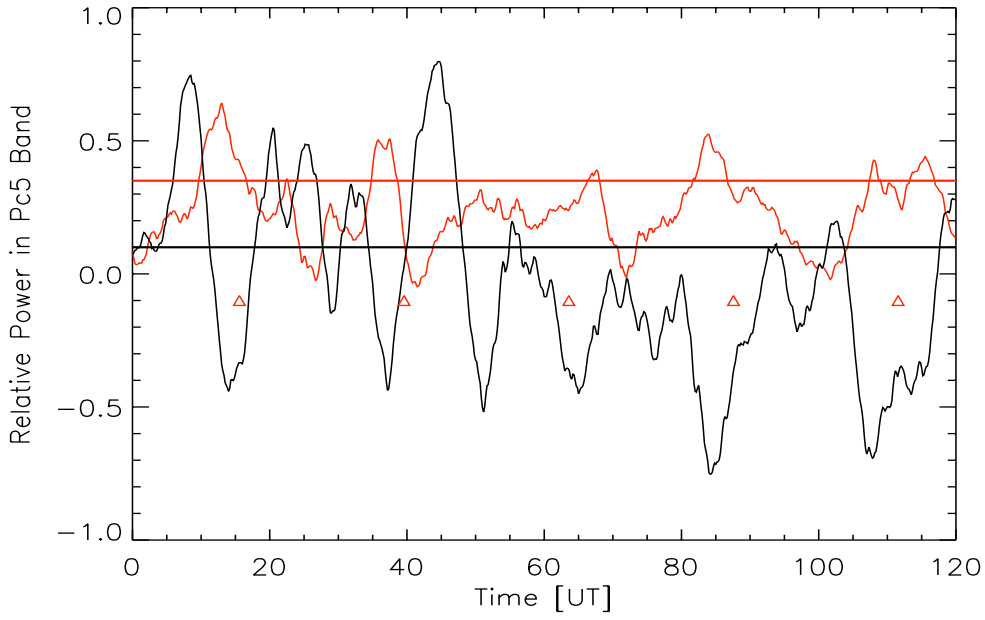

Figure 3.15 The relative power of the long period band (black) at SPA overlaid onto the relative power of the Pc5 band (red) there. Open field lines exist when both curves exist under their respective noise floors.

3.3 The BATSRUS Space Weather Model

Open-closed boundary computational results of the space weather model developed at the University of Michigan, referred to as the Block Adaptive-Tree Solar-wind Roe-type Upwind Scheme (BATSRUS), are compared with ground-based magnetometer observations. To date, due to the model's extreme computational time, BATSRUS has only been run for two pre-storm days; while it cannot yet be said whether the model holds up under the disturbed conditions associated with a corotating interaction region, the model is almost perfectly in agreement with observations of the open-closed boundary, specifically in reference to the noise-floor criteria listed above.

In the below simulation images, BATSRUS' computationally defined OCB is juxtaposed with observational results, which are represented by the color of the square dots, which represent the four fluxgates (P2, P3, MCM, and SPA) at various times. A red dot indicates a closed line, while green represents open. If BATSRUS is accurate, all dots within its OCB should be open (green), while all those in the exterior should be closed (red). This is mostly the case, with one minor exception and one very peculiar exception. The minor exception occurs at Time=38.333 (bottom-left panel); this exception is most probably due to the agreed upon noise-floor designation and will be further looked into. The peculiar exception occurs at Time=15.500. This is much harder to account for and casts serious doubt onto the current noise-floor designation. A more rigorous and quantitative description of the noise floor is currently being looked into.

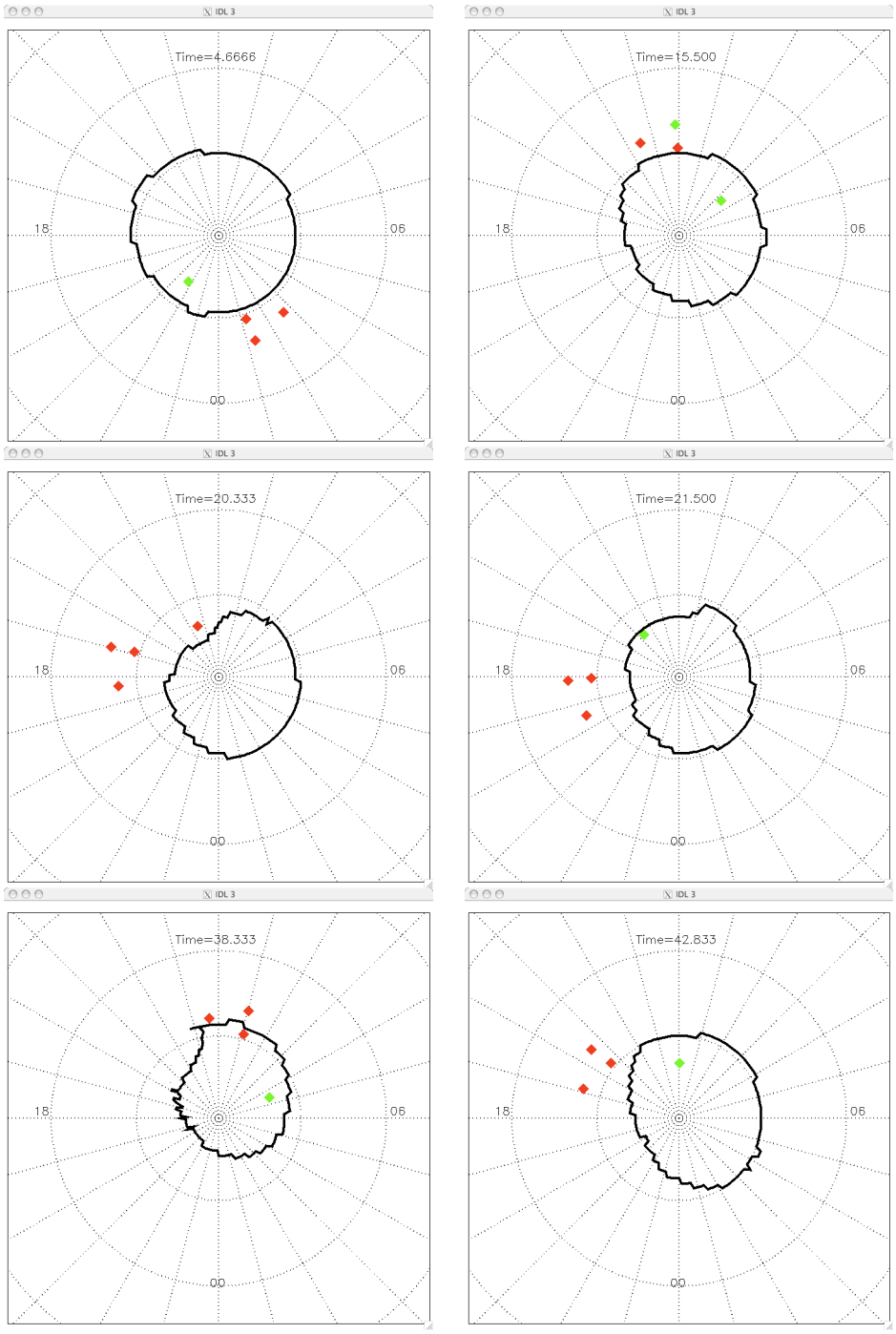

Figure 3.16 BATSRUS OCB simulations juxtaposed with observational results.

CHAPTER 4

CONCLUSIONS AND OUTLOOK

During the summer of 2008, solar cycle 23 neared the end of its declining phase, a historically quiet period of solar activity. With little solar activity, researchers were able to study the impact of a corotating interaction region on the magnetosphere and, specifically, how a CIR modulates the open-closed boundary of the magnetosphere by spectral analysis of data streams obtained by the PENGUIn AGOs network of ground-based magnetometers on the Antarctic continent. By tracking Pc5 modes in the power spectra, researchers were able to monitor the dynamic behavior of the leading edge of closed field lines bordering the OCB and compare observations with results provided by the BATSRUS space weather model. It was strongly suggested that such synoptic magnetometer data sets can be used to validate the accuracy of BATSRUS during these CIR-driven storms, although currently only pre-storm days have been simulated due to the extreme computational time of the model at the resolution required. From these early results however, it is demonstrated that the current criteria being used to define the noise floor must be made more rigorously and quantitatively, which is being looked into. At the time of this writing, the BATSRUS model is currently being run to simulate days during the CIR-induced geomagnetic storm. Researchers plan to use improved noise floor criteria to evaluate the accuracy of BATSRUS' depiction of OCB modulation during CIR-driven geomagnetic storms.

APPENDIX A

NOAA SPACE WEATHER SCALE FOR GEOMAGNETIC STORMS

This table serves as a reference for the associated geomagnetic activitiy and technological impact at various Kp levels.

Scale	Effects (duration of event will influence severity of effects)	Physical measure
G 5 Extreme	Power systems: widespread voltage control problems and protective system problems can occur; some grid systems may experience complete collapse or blackouts. Transformers may experience damage. Spacecraft operations: may experience extensive surface charging, problems with orientation, uplink/downlink and tracking satellites. Other systems: pipeline currents can reach hundreds of amps, HF (high frequency) radio propagation may be impossible in many areas for one to two days, satellite navigation may be degraded for days, low-frequency radio navigation can be out for hours, and aurora has been seen as low as Florida and southern Texas.	Kp = 9
G 4 Severe	Power systems: possible widespread voltage control problems and some protective systems will mistakenly trip out key assets from the grid. Spacecraft operations: may experience surface charging and tracking problems, corrections may be needed for orientation problems. Other systems: induced pipeline currents affect preventive measures, HF radio propagation sporadic, satellite navigation degraded for hours, low-frequency radio navigation disrupted, and aurora has been seen as low as Alabama and northern California (typically 45° geomagnetic lat.).	Kp = 8 (or a 9-)
G 3 Strong	Power systems: voltage corrections may be required; false alarms triggered on some protection devices. Spacecraft operations: surface charging may occur on satellite components, drag may increase on low-Earth-orbit satellites, and corrections may be needed for orientation problems. Other systems: intermittent satellite navigation and low-frequency radio navigation problems may occur, HF radio may be intermittent, and aurora has been seen as low as Illinois and Oregon (typically 50° geomagnetic lat.).	Kp = 7
G 2 Moderate	Power systems: high-latitude power systems may experience voltage alarms; long-duration storms may cause transformer damage. Spacecraft operations: corrective actions to orientation may be required by ground control; possible changes in drag affect orbit predictions. Other systems: HF radio propagation can fade at higher latitudes, and aurora has been seen as low as New York and Idaho (typically 55° geomagnetic lat.).	Kp = 6
G 1 Minor	Power systems: weak power grid fluctuations can occur. Spacecraft operations: minor impact on satellite operations possible. Other systems: migratory animals are affected at this and higher levels; aurora is commonly visible at high latitudes (northern Michigan and Maine).	Kp = 5

APPENDIX B

GLOSSARY

A-Index	A daily average level for geomagnetic activity, based on the K-index. (See Ak-Index.)
ACE	Acronym: Advanced Composition Explorer.
Active Region	A localized, transient volume of the solar atmosphere in which sunspots, flares, etc., may be observed. Active regions are the result of enhanced magnetic fields; they are bipolar and may be complex if the region contains two or more bipolar groups.
AGOs	Acronym: Automated Geophysical Observatories
Ak-Index	A 3-hourly "equivalent amplitude" index of geomagnetic activity for a specific station or network of stations (represented generically here by k) expressing the range of disturbance in the horizontal magnetic field. "Ak" is scaled from the 3-hourly K index according to the following table:

K	0	1	2	3	4	5	6	7	8	9
Ak	0	3	7	15	27	48	80	140	240	400

AU	The mean distance between the Earth and Sun equal to 1.496 x10"m
Auroral Zone	A ring-shaped region encompassing either geomagnetic pole within which maximum of auroral activity takes place.
BATSRUS	Acronym: Block Adaptive-Tree Solar-wind Roe-type Upwind Scheme.
Conjugate Points	Two points on the Earth's surface at opposite ends of a geomagnetic field line.
Coordinated Universal Time (UTC)	By international agreement, the local time at the prime meridian, which passes through Greenwich, England. It was formerly known as Greenwich Mean Time, or sometimes simply Universal Time. There are 24 time zones around the world, labeled alphabetically. The time zone centered at Greenwich has the double designation of A and Z.
Corona	The outermost layer of the solar atmosphere, characterized by low densities ($< 10^9$ cm^{-3}) and high temperatures ($> 10^6$ K).
Coronal Hole	An extended region of the corona, exceptionally low in density and associated with unipolar photospheric regions having "open" magnetic field topology. Coronal holes are largest and most stable at or near the solar poles, and are a source of high-speed solar wind. Coronal holes are visible in several wavelengths. Transequatorial coronal holes are the source of many recurrent geomagnetic disturbances since their lifetimes are months to years. The solar wind emanating from these holes is characteristically high in velocity and low in density.

Coronal Mass Ejection (CME)

An outflow of plasma from or through the solar corona. CMEs are often, but not always, associated with erupting prominences, disappearing solar filaments, and/or flares. CMEs vary widely in structure, density, and velocity. Large and fast CMEs can approach densities of 10^{16} g and velocities of 2000 km/s. Earth impacting CMEs can result in significant geomagnetic storms.

Corotating Interaction Region (CIR)

Large-scale plasma structures in the solar wind generated in low- and mid-heliospheric latitudes by the interaction of a fast solar wind driving a slow solar wind and lasting throughout multiple solar rotations.

Corrected Geo-magnetic Coordinates (CGM)

A nonspherical coordinate system based on a magnetic dipole axis that is offset from the Earth's center by about 502 km toward a location in the Pacific Ocean (20.4° N 147.3° E). This "eccentric dipole" axis intersects the surface at 82° N 90° W, and 75° S 119° E.

Cusps (aka Polar Cusps)

In the magnetosphere, two regions near magnetic local noon and approximately 15 degrees of latitude equatorward of the north and the south magnetic poles. The cusps mark the division between geomagnetic field lines on the sunward side (which are approximately dipolar but somewhat compressed by the solar wind) and the field lines in the polar cap that are swept back into the magnetotail by the solar wind.

Dynamics Pressure

The momentum flux (P) of the solar wind. P=(density)* (velocity)^2 where density is in particles/cm^3 and velocity is in km/s.

Flux

The rate of flow of a physical quantity through a reference surface.

Geomagnetic Activity

Natural variations in the geomagnetic field classified quantitatively into quiet, unsettled, active, and geomagnetic storm levels according to the observed A-index:

quiet	0 - 7
unsettled	8 - 15
active	16 - 29
minor storm	30 - 49
major storm	50 - 99
severe storm	100 - 400

Geomagnetic Field Components

The vector components of the geomagnetic field at the surface of the Earth. These elements are usually denoted thus in the literature:

X = the geographic northward component
Y = the geographic eastward component
Z = the vertical component, reckoned positive downward
H = the horizontal intensity, of magnitude = $(X^2 + y^2)^{1/2}$
F = the total intensity = $(H^2 + Z^2)^{1/2}$
I = the inclination (or dip) angle = arctan(Z/H)
D = the declination angle (measured from the geographic north direction to the H component direction, positive in an eastward direction) = arctan (Y/X)

However, in NOAA usage and magnetometer lingo, the geomagnetic northward and geomagnetic eastward components are called the H and D components

Geomagnetic Field	The magnetic field in and around the Earth. The intensity of the magnetic field at the Earth's surface is approximately 32,000 nT at the equator and 62,000 nT at the north pole (the place where a compass needle points vertically downward). The geomagnetic field is dynamic and undergoes continual slow secular changes as well as short-term disturbances (see geomagnetic activity). The geomagnetic field can be approximated by a centered dipole field, with the axis of the dipole inclined to the Earth's rotational axis by about 11.5 degrees. Geomagnetic dipole north is near geographic coordinate 79 degrees N and 71 degrees W (near Thule, Greenland), and dipole south is near 79 degrees S and 110 degrees E (near Vostok, Antarctica). The observed or dip poles, where the magnetic field is vertical to the Earth's surface, are near 77 degrees N and 102 degrees W, and 65 degrees S and 139 degrees E. The adopted origin of geomagnetic longitude is the meridian passing through the geomagnetic poles (dipole model) and the geographic south pole. (See also corrected geomagnetic coordinates.)
Geomagnetic Storm	(1) A worldwide disturbance of the Earth's magnetic field, distinct from regular diurnal variations. A storm is precisely defined as occurring when the daily Ap index exceeds 29, or (2) NOAA Space Weather Scale (G) for geomagnetic storm disturbances.
Geospace	An umbrella term for the near-Earth region of outer space that includes the upper-atmosphere, the ionosphere, and the magnetosphere.
GOES	Acronym: Geostationary Operational Environment Satellite
Interplanetary Magnetic Field (IMF)	The magnetic field carried with the solar wind.
Invariant Magnetic Latitude	The geomagnetic latitude at which a particular line of force of the geomagnetic field, characterized by L (the altitude of the field line at the equator), intersects the Earth.
Ionosphere	The region of the Earth's upper atmosphere containing free electrons and ions produced by ionization of the constituents of the atmosphere by solar ultraviolet radiation at short wavelengths < 100nm) and energetic precipitating particles. The ionosphere influences radio wave propagation of frequencies less than about 300 MHz.
K Index	A 3-hourly quasi-logarithmic local index of geomagnetic activity relative to an assumed quiet-day curve for the recording site. Range is from 0 (quiet) to 9 (severely disturbed). The K index measures the deviation of the most disturbed component (see geomagnetic elements).
Kp Index	A 3-hourly planetary index of geomagnetic activity calculated by the Institut fur Geophysik der Gottingen Universitat, Germany, from the K indexes observed at 13 stations primarily in the Northern Hemisphere. The Kp indexes, which date from 1932, are used to determine the Ap indexes.
L1	Lagrangian orbit number 1. A location on the Earth/ Sun line where gravitational forces can be balanced to maintain a stable orbit. Approximately 1.5 million km upstream of the Earth. Solar wind monitors located there allow a 20-60 minute (depending on solar wind velocity) warning of geomagnetic disturbances at Earth. (This is where ACE collects data.)
Magnetic Local Time (MLT)	On Earth, analogous to geographic local time. MLT at a given location is determined by the angle subtended at the geomagnetic axis between the geomagnetic midnight meridian and the meridian that passes through the location. 15 degrees = 1 h. The geomagnetic meridian containing the sub-solar point defines geomagnetic local noon, and the opposite meridian defines geomagnetic midnight.
Magnetopause	The boundary surface between the solar wind and the magnetosphere, where the pressure

	of the Earth's magnetic field effectively equals the dynamic pressure of the solar wind.
Magnetosheath	The region between the bow shock and the magnetopause, characterized by very turbulent plasma. For the Earth, along the Sun-Earth axis, the magnetosheath is about 2 Earth radii thick.
Magnetosphere	The magnetic cavity surrounding a magnetized body, carved out of the passing solar wind by virtue of the magnetic field, which prevents, or at least impedes, the direct entry of the solar wind plasma into the cavity.
Magnetotail	The extension of the magnetosphere in the antisunward direction as a result of interaction with the solar wind. In the inner magnetotail, the field lines maintain a roughly dipolar configuration. At greater distances, the field lines are stretched into northern and southern lobes, separated by a plasmasheet. There is observational evidence for traces of the Earth's magnetotail as far as 1000 Earth radii downstream.
NOAA	Acronym: National Oceanic and Atmospheric Administration
Noise Floor	The measure of the signal created from noise sources and unwanted signals within a measurement system.
nT	nanotesla = 10^{-9} Tesla
Pc 5 Mode	A geomagnetic micropulsation, usually of solar origin, with a period ranging between 150-600 seconds.
PENGUIn	Acronym: Polar Experiment Network for Geophysical Upper-atmosphere Investigations
Plasma	A gas that is ionized sufficiently to be a good electrical conductor and be affected by magnetic fields.
Power Spectrum	A display of the frequency content of a signal.
(Geo-magnetic) Pulsation	A rapid fluctuation of the geomagnetic field having periods from a fraction of a second to tens of minutes and lasting from minutes to hours. There are two main patterns: Pc (a continuous, almost sinusoidal pattern), and Pi (an irregular pattern). Pulsations occur at magnetically quiet as well as disturbed times.
Shock	A discontinuity in pressure, density, and particle velocity, propagating through a compressible fluid or plasma.
Solar Maximum	The month(s) during a sunspot cycle when the smoothed sunspot number reaches a maximum.
Solar Minimum	The month(s) during a sunspot cycle when the smoothed sunspot number reaches a minimum.
Solar Wind	The outward flow of solar particles and magnetic fields from the Sun. Typically at 1 AU, solar wind velocities are near 375 km/s and proton and electron densities are near 5 cm^{-3}. The total intensity of the interplanetary magnetic field is nominally 5 nT.
STEREO	Acronym: Solar TErrestrial RElations Observatory.
Substorm	A geomagnetic perturbation lasting 1 to 2 hours, which tends to occur during local post-midnight nighttime. The magnitude of the substorm is largest in the auroral zone,

	potentially reaching several thousand nanotesla. A substorm corresponds to an injection of charged particles from the magnetotail into the auroral oval.
Troposphere	The lowest layer of the Earth's atmosphere, extending from the ground to the stratosphere at approximately 13 km of altitude.
Universal Time (UT)	A shortened form of the more correct Coordinated Universal Time (UTC).

* This glossary is largely owed to NOAA's online glossary, which can be found in its entirety at: http://www.swpc.noaa.gov/info/glossary.html; some entries have been edited for brevity and relevance.

REFERENCES

Birn, J., E. W. Hones, Jr., J. D. Craven, L. A. Frank, R. D. Elphinstone, and D. P. Stern (1991), On Open and Closed Field Line Regions in Tsyganenko's Field Model and Their Possible Associations with Horse Collar Auroras, 96(A3), 3811-3817.

Choi, Y., Y. J. Moon, S. Choi, J.-H. Baek, S. Kim, K. S. Cho, and G. Choe (2009), Statistical Analysis of the Relationships among Coronal Holes, Corotating Interaction Regions, and Geomagnetic Storms, Solar Physics, 254(2), 311-323.

Dudeney,, J. R., R. I. Kressman, A. S. Rodger (1998), Automated observatories for geospace research in the polar regions, Antarctic Science, 10 (2), 192-203

Forsyth, R. J, E. Marsch (1999), Solar origin and interplanetary evolution of stream interfaces, Space Science Reviews, 89, 7-20.

Gonzalez, W. D., B. T. Tsurutani, F. Tang (1996), The solar and interplanetary causes of geomagnetic activity and quiet, Solar Drivers of Interplanetary and Terrestrial Disturbances, ASP Conference Series, 95, 453-460.

Gonzalez, W. D., J. A. Joselyn, Y. Kamide, H. W. Kroehl, G. Rostoker, B. T. Tsurutani, and V. M. Vasyliunas (1994), What is a Geomagnetic Storm?, J. Geophys. Res., 99(A4), 5771-5792.

Heber, B., T. R. Sanderson, and M. Zhang (1999), Corotating interaction regions, Advances in Space Research, 23(3), 567-579.

Jacobs, J. A. (1970), Geomagnetic Micropulsations, Springer-Verlag, New York.

Kamide, Y., et al. (1998), Current understanding of magnetic storms: storm-substorm relationships, Journal of Geophysical Research, 103, A8, 17705-17728.

Lanzerotti, L. J. (2002), Solar Terrestrial Physics, in Encyclopedia of Physical Science and Technology, edited, Academic Press.

Lanzerotti, L. J., A. Shono, H. Fukunishi, and C. G. Maclennan (1999), Long-period hydromagnetic waves at very high geomagnetic latitudes, J. Geophys. Res., 104(A12), 28423-28435.

Lessard, M. R., et al. (2009), PENGUIn multi-instrument observations of dayside high-latitude injections during the 23 March 2007 substorm, J. Geophys. Res., 114(A1), A00C11.

Mason, G. M., et al. (1999), Origin, Injection, and Acceleration of CIR Particles: Observations Report of Working Group 6, Space Science Reviews, 89(1), 327-367.

Mende, S. B., et al. (2009), Observations of Earth space by self-powered stations in Antarctica, Review of Scientific Instruments, 80, 124501.

Morley, S. K. (2008), Observations of magnetospheric substorms during the passage of a corotating interaction region, paper presented at Proc. of the 7th Aust. Space Sci. Conf. 2007, Australia.

Ohmi, T., et al. (2004), Origin of the slow solar wind, Advances in Space Research, 33, 689-695.

Richardson, I. G., H. V. Cane, and E. W. Cliver (2002), Sources of geomagnetic activity during nearly three solar cycles (1972-2000), J. Geophys. Res., 107(A8), 1187.

Richardson, I. G., et al. (2006), Major geomagnetic storms (Dst ≤ -100 nT) generated by corotating interaction regions, J. Geophys. Res., 111(A7), A07S09.

Riley, P. (2007), Modeling corotating interaction regions: From the Sun to 1 AU, Journal of Atmospheric and Solar-Terrestrial Physics, 69(1-2), 32-42.

Rosenberg, T. J. , J. H. Doolittle (1994), Studying the polar ionosphere and magnetosphere with automatic geophysical observatories: the U. S. program in Antarctica, Antarctic Journal of the United States, 29(5), 3.

Russell, C. T. (2004), Outer planet magnetospheres: a tutorial, Advances in Space Research, 33(11), 2004-2020.

Russell, C. T. (2001), Solar wind and interplanetary magnetic field: a tutorial, Space Weather, Geophys Mono. Series, 125, ed. by P. Song, H. J. Singer, and G. L. Siscoe, 73-89.

Toth, G. V., O.; Ridley, A. J.; Gombosi, T. I.; de Zeeuw, D.; Hansen, K. C.; Chesney, D. R.; Stout, Q. F.; Powell, K. G.; Kane, K. J.; Oehmke, R. C. A Physics-Based Software Framework for Sun-Earth Connection Modeling.

Tsurutani, B. T., et al. (2006), Corotating solar wind streams and recurrent geomagnetic activity: A review, 111(A7), A07S01.

Tsurutani, B. T., Solar/Interplanetary Plasma Phenomena Causing Geomagnetic Activity at Earth, in Proceedings of the International School of Physics "Enrico Fermi," ed. by B. Coppi, A. Ferrari, and E. Sindoni, IOS Press, Amsterdam, 2000.

Wolf, R. A., R. W. Spiro, S. Sazykin, and F. R. Toffoletto (2007), How the Earth's inner magnetosphere works: An evolving picture, Journal of Atmospheric and Solar-Terrestrial Physics, 69(3), 288-302.